NASA Technical Paper 2541

1986

Experimental Study of the Effects of Installation on Single- and Counter-Rotation Propeller Noise

P. J. W. Block

Langley Research Center
Hampton, Virginia

NASA
National Aeronautics
and Space Administration

Scientific and Technical Information Branch

Contents

Summary

To understand the effects of installation on propeller noise, numerous measurements are required to define the directivity as well as the level of the noise. An experimental study was conducted in a wind tunnel to map the noise radiation pattern for various single-rotation (SR) propeller and counter-rotation (CR) propeller installations. The measurements covered ±60° from the propeller disk plane and ±60° in the cross-stream direction. Configurations examined included SR and CR propellers at angle of attack and an SR pusher installation. The increases in noise that arise from an unsteady loading operation such as an SR pusher or a CR exceeded 15 dB in the forward axial direction and in addition strongly depended on the observer location. Most of the additional noise appears to radiate in the axial directions for unsteady loading operations of both the SR pusher and the CR tractor.

Introduction

Recent studies have shown that turboprop aircraft offer significant fuel savings over turbofan aircraft (ref. 1). Therefore, future aircraft propulsion systems will incorporate such advanced propeller concepts as highly swept and tapered blades and counter-rotation propellers mounted in pusher or tractor configurations. However, the noise levels from these propellers raise both design and environmental concerns. What will the acoustic loads be on the aircraft structure? Will these aircraft meet the lowering noise regulations in the far field? Can acceptably low cabin noise levels be maintained without severe weight penalties? To assess the noise impact, near-field and far-field propeller noise measurements are needed on advanced propeller installations. These measurements will be used to validate available propeller noise prediction methods for steadily loaded propellers and to aid in modifying these theoretical models to represent the unsteady loading on the propeller blades due to installation effects.

Little information is available on the noise produced by a propeller operating in an installed environment, such as at nonzero pitch (α), in an airfoil wake (pusher installation), or for counter-rotation propellers. References 2 through 5 are examples of experimental studies aimed at quantifying these installation effects. In reference 2 Tanna et al. conclude from their study of a wing-mounted tractor installation that both discrete-frequency and broadband noise increases as propeller pitch changes from 0° to 10°. Although the data for this study were limited to a 70° arc at only two azimuthal angles (one directly under the propeller and one 30° below the plane of the wing), they show a directional dependence; that is, the amount of noise increase depends on the location of the measurement. More data would be necessary to adequately define the complete directivity pattern. An early attempt to measure the noise from a pusher propeller is reported by Herkes in reference 3. Unfortunately these noise measurements were made in a hard-walled tunnel. Herkes points out that the data were seriously affected by floor reflections and that although a large degree of irrepeatability was encountered, "an increase of the overall sound pressure level was obvious as the wing was moved quite close to the propeller." Another pusher propeller noise experiment was conducted in an anechoic flow environment and is reported by the author in reference 4. This study concludes that at the introduction of a wake (pusher installation) the propeller noise generally increased in OASPL, increased in harmonic content, and displayed an azimuthal dependence. It was also shown that the increase in noise was inversely proportional to propeller thrust; however, measurements were made in only six directions in reference 4. In reference 5 Hubbard studied the noise from counter-rotation propellers and also shows unique azimuthal directivity of the noise. He notes that the maximum sound pressures "occur at the axis of overlap." All these experimental studies show that the unsteadily loaded propeller produces an additional source of noise, and three of them show that the noise has a definite directivity. An analytical study reported by Runyan in reference 6 showed that introducing a perturbation to the propeller loading produces a contribution to the propeller noise that becomes increasingly important as the observation point moves from the propeller plane to the propeller axis. Thus to capture or more completely define the effect of the unsteady loading that is introduced with installation, many measurements covering a wide observer domain are necessary. The present paper addresses this area with an experimental study designed to define the noise radiation patterns of single-rotation propellers and counter-rotation propellers in a representative set of installed environments. Some data from this experimental study have been published with theory comparisons in references 7, 8, and 9. The experimental setup is described in detail in reference 10. A complete data summary is contained herein.

The configurations considered in this study include sting-mounted single-rotation (SR) propellers and counter-rotation (CR) propellers at zero and nonzero pitch. Also a pylon-mounted SR pusher installation was studied. The propellers were the straight-bladed SR-2 design. The test matrix was divided into two operating conditions: lightly loaded

with a high tip Mach number and more heavily loaded with a low tip Mach number. A remotely controlled microphone carriage was used to map the noise radiation patterns over a rectangular area extending from 60° in front of the propeller disk to 60° behind it and about 60° to either side of the propeller axis. Noise data over this rectangle are presented in color-coded contour plots.

Symbols

a_n, b_n, c_n	Fourier coefficients
C_T	thrust coefficient
J	propeller advance ratio
M_T	helical tip Mach number
R	propeller radius
r	distance from propeller axis to an elemental section on the propeller blade
α	pitch angle of the propeller (see fig. 4)
β	geometric pitch of the propeller airfoil sections with respect to the plane of rotation
$\beta_{.75}$	geometric pitch of propeller airfoil sections at $r/R = 0.75$
θ	angle of the microphone array with respect to the propeller plane of rotation (see fig. 7)
ϕ	azimuthal angle of a line of microphone measurements with respect to the vertical (see fig. 7)
ψ	yaw angle of the propeller axis (see fig. 4)

Abbreviations:

BPF	blade passage frequency
CR	counter rotation
OASPL	overall sound pressure level
OTS	open test section
rps	revolutions per second
SPL	sound pressure level
SR	single rotation

Description of the Experiment

Hardware

Propellers. The SR-2 propeller design was employed in this study. The chord and twist (β) distributions of this design are given in figure 1. A representative set of airfoil sections for the SR-2 propeller is given in figure 2. The blades were fabricated from aluminum on a numerically controlled milling machine and were dynamically balanced after assembly with the spinner and hub. All propeller configurations were driven by a single, 29-hp, 10 000-rpm electric motor.

The SR propeller was 16.9 in. (0.429 m) in diameter, and the blade pitch angles were adjustable in increments of 1°. To set the angle, a pin was placed in a labeled hole in the hub. With this arrangement, the collective blade angle was exactly repeatable. The SR propeller was generally tested with four blades, but one sequence of runs was performed with eight blades.

The SR-2 surface coordinates were modified when fabricating the CR propeller. The CR coordinates were obtained by scaling the SR propeller coordinates down by a factor of 0.88757 to a diameter of 15.0 in. (0.381 m). The blades were then shifted out radially 0.552 in. (0.014 m). The resultant diameter of the CR propeller was 16.104 in. (0.409 m). The hub for the CR propeller permitted a continuous range of blade angle settings. The collective blade angle for one row of blades was set to an accuracy of ±0.25° with a blade mold fixture and protractor. For the tests described herein, each disk of the CR propeller had four blades and the same pitch setting ($\beta_{.75}$). The pitch change axes of the two rows of blades were separated by 2.31 in. (0.059 m). The two CR hubs were geared together so that there were eight azimuthal positions where the blades appeared to overlap, or "cross over," to an observer standing in front of the propeller. These directions were spaced every 45° beginning 24° counterclockwise from the vertical looking downstream.

Nacelle, pylon, and sting. The nacelle was a tapered cylinder with a maximum outside diameter of 6.0 in. (0.15 m). The hub diameter was 4.5 in. (0.11 m). A scaled drawing of the propellers, nacelle, and pylon, or strut, is shown in figure 3 in the various test configurations. The CR nacelle was longer than the SR nacelle to allow space for the additional hub and blades and associated gearbox. There were two mounts for the nacelle: the sting mount, in which the nacelle was an aerodynamic extension of the straight sting, and the pylon mount, in which the nacelle was attached to a pylon extending downward from the sting via an adapter plate. There were two configurations for the nacelle in the pylon mount: tractor (propeller precedes the pylon) and pusher (propeller follows the pylon). The spinner and nacelle coordinates for the SR propeller are given in table 1.

The pylon was a tapered NACA 0012 airfoil. The chord length above the nacelle was 12.5 in. (0.318 m),

and below the nacelle it was 10 in. (0.254 m). The center of the pylon was 17.5 in. (0.445 m) from the propeller plane in both the pusher and the tractor configurations.

The experimental setup was such that the propeller pitch (α), and yaw (ψ) could be changed without changing the position of the center of the propeller disk. The center of the propeller disk was kept 35.0 in. (0.889 m) above the microphone carriage. Figure 4 defines the axes of pitch and yaw.

Microphone carriage. In concept the microphone carriage was a movable floor mounted above the tunnel floor and supporting a much smaller and constant thickness boundary layer. It was designed to circumvent the contamination of the acoustic data caused by reflections from the tunnel floor while providing the capability of making numerous streamwise noise measurements covering a wide area. A large size was required to minimize edge diffraction at the lowest frequency of interest (400 Hz). In figure 4 the carriage and the propeller, in the pylon-mounted tractor configuration, are shown.

The carriage was a streamlined plate of rectangular planform holding an array of 11 flush-mounted microphones. It was 72 in. (1.8 m) wide (streamwise), 168 in. (4.27 m) long (cross-stream dimension), and 2.30 in. (0.0584 m) thick. It had a rigid foam core and an aluminum skin bonded together with an epoxy adhesive. A wooden beam running spanwise down the center of the chord was used for microphone mounting. The microphones were fit into phenolic holders, which were secured to the wooden beam. A sketch of the carriage showing the microphone locations is given in figure 5. An accelerometer was mounted under the carriage to monitor the vibration levels of the microphone support beam. The microphones, labeled 1 through 11, were positioned at nominal increments of 12.5° in the cross-stream direction (azimuthally) from the propeller axis, which was maintained at 35.0 in. (0.889 m) above the carriage for all test conditions.

The carriage was moved in the streamwise direction on Thompson bearings and a set of 1-in-diameter (0.025-m) stainless steel rods (see fig. 4). The carriage was remotely controlled and was positioned at 13 fixed streamwise locations, which corresponded to nominal increments of 10° from the propeller disk plane, beginning at 60° in front of the disk plane and ending 60° behind for the reference configuration (sting-mounted SR propeller at $\alpha = 0°$). Two additional locations were added for two runs with the CR propellers, to measure the noise at 72° and 78° in front of the disk plane. Thus, the noise radiation pattern for each of the propeller configurations was measured at a minimum of 143 locations on a rectangular grid covering the range of ±60° streamwise and about 60° laterally (cross stream) from the propeller axis. Dimensionally this grid covered 10.4 ft (3.17 m) in the streamwise direction and 9.54 ft (2.91 m) in the cross-stream direction.

Facility

The tests were conducted in the Langley 4- by 7-Meter Tunnel. This is a closed, single-return, atmospheric wind tunnel allowing operation with an open or closed test section. A more detailed description of this facility and an acoustic evaluation of the open test section (OTS) are given in reference 11. Figure 6 is a plan view of the OTS showing the size of the microphone carriage, the array of microphones, and the propeller plane location. The shaded region in the center is the area over which the propeller noise radiation patterns were mapped. Also shown in figure 6 are the locations of the acoustic treatment. The treatment consisted of open cell foam bats 6 in. (0.152 m) thick applied to the raised ceiling, sidewalls, and control room wall. A tone burst calibration of the OTS showed that within the dynamic range of the recording instrumentation, the microphone systems were not able to detect reflections from these surfaces.

Test Conditions

Test matrix. Table 2 gives the conditions at which data were acquired in this test. All data were obtained at a tunnel dynamic pressure of 12 psf (575 Pa), which gave a nominal tunnel speed of 100 fps (30.48 m/s). The run numbers given in the first column uniquely describe the hardware and operating speed and are used in the data figures.

The SR and CR propellers were each tested with four blades per disk or per row. An eight-bladed SR propeller was also tested to provide a comparison with the CR propeller consisting of two four-bladed disks, in which the total number of blades is the same. The propeller blade pitch and rotational speeds were chosen to emphasize either the thickness noise or the loading noise and are discussed below. To examine the effect of simply changing the angle of attack of the propeller shaft or axis, the noise of the sting-mounted SR and CR propellers was mapped at $\alpha = -8°$, 0°, and 8°. For these runs the height of the propeller was held at 35.0 in. (0.889 m) above the microphone carriage; however, the axial location did shift slightly (see ref. 10). The pylon-mounted SR propeller was also tested with its axis yawed ($\psi = -10°$) with the center of the disk kept at the same location. Figure 4 defines the direction of α and ψ.

Propeller operating conditions. The forward, or axial, speed for all runs was nominally 100 fps (30.48 m/s). The tunnel air temperature (refer to ref. 10) varied from 43°F to 69°F (6.1°C to 20.6°C), and the air density from 0.00228 to 0.00239 slug/ft^3 (1.18 to 1.23 kg/m^3). Table 3 lists the propeller advance ratios, helical tip Mach numbers, and measured thrust at selected conditions. Two blade pitch angles $\beta_{.75}$ were tested. These were chosen to provide efficient propeller operation at the relatively low forward speed (100 fps) that was acoustically acceptable in the wind tunnel and high rotational tip speed (800 fps (243 m/s)) necessary to simulate full-scale rotational tip speeds. The 12.7° blade setting was used at high rotational speeds, which were designed to maximize the thickness source of noise. The 20.6° setting was used at lower rotational speeds, which were selected to maximize the propeller loading source of noise. Because of the power limitation of the motor, these conditions are still considered to relatively lightly load the propeller, although the propeller section local angles of attack are representative of typical propeller operation. At each blade setting, generally two rotational speeds were examined: one at the predicted peak efficiency and one slightly higher to increase the loading of the propeller without stalling it. The data are arranged as either a high- or a low-tip-speed operating condition.

Data Reduction and Presentation

The microphone data were high-pass filtered at 80 Hz and FM recorded on 1-in. magnetic tape at 60 ips. A triple redundancy system was employed for recording the microphone attenuator settings to minimize data loss. A once-per-revolution pulse, which was generated by a magnetic sensor on the shaft, was also recorded for data analysis purposes. The recorded data were digitized using the once-per-revolution pulse to obtain 512 points of data for each revolution of the shaft. A minimum of 120 revolutions of data were stored for each microphone (61 440 points).

The data were analyzed in the time and the frequency domain. In the time domain an average time history, or mean signal per revolution, was computed by averaging the sampled pressure signal over the 120 revolutions of the shaft. The data presented herein were analyzed in the frequency domain by the following method. Each revolution of data was Fourier analyzed to produce the sine and cosine coefficients for the first 25 harmonics of the blade passage frequency (BPF) (a_n and b_n, respectively, for $n = 1, 2, \ldots, 25$). These coefficients were averaged over the 120 revolutions of data to yield $\bar{a}_n$ and $\bar{b}_n$. The root mean square (rms) amplitude of the noise contribution for each of the harmonics is computed from these by using

$$c_n = \left(\bar{a}_n^2 + \bar{b}_n^2\right)^{1/2}$$

and converted to decibels. These harmonic levels were computed for each of the 143 microphone locations. The OASPL for each microphone location was computed as the sum of the mean square values of each of the harmonics.

For ease of comparison and presentation, the data have been corrected to free-field levels by simply subtracting 6 dB from the measured pressure levels to account for pressure doubling at the hard surface. These free-field levels were then normalized to a constant radius of 35 in. (0.889 m) using the ratio of the distances from the propeller disk center. A distance of 35 in. corresponds to the closest measurement point. The data levels are then displayed on the rectangular grid indicated in figure 7. The levels are displayed in decibels using color-coded contour plots. The color bar scale at the top of the chart gives the noise level. The scale is graduated in 1-dB increments and always covers a 30-dB range. The maximum value on the scale changes to accommodate the range of levels for the particular operating condition and was chosen to allow comparison between cases of similar operating conditions. This maximum value is also given in table 2. In the charts the small plus signs indicate the microphone locations. The airflow is from left to right, so the first column of pluses in each chart represents the microphone array location 60° upstream of the propeller disk plane, and the last column, 60° downstream (see fig. 6). The size, location, and orientation of the propeller disk plane are indicated on the charts. These plots present the data corrected to free field, normalized to constant radius, and then displayed on the grid defined by the 143 microphone locations. To achieve a smooth representation, the 143 measurements were fit with a two-dimensional cubic spline having zero tension (ref. 12). Additional interpolated values were then calculated and the matrix of data was enriched from 11 (microphones) × 13 (streamwise stops) to a 50×50 matrix of evenly spaced points. This method gave an accurate representation of the data at the measurement points. The data presented in this format include the OASPL and the SPL's (in decibels) of the first four harmonics of the blade passage frequency (BPF) c_n ($n = 1, 2, 3, 4$). For the cases contained herein, the first four harmonics account for most of the OASPL. In this paper the fundamental frequency, or BPF, is also called the first harmonic. Also, given in the figures are the advance ratio J, the thrust coefficient C_T, and the helical tip Mach number M_T.

Results

The data are presented using color-coded contour plots. A color bar scale is given with the data to show the noise levels in decibels.

Tractor Installations at 0° Pitch

Sting-mounted, four-bladed SR propeller. The sting-mounted SR propeller with four blades represents the baseline, or uninstalled, configuration (see fig. 3). Here the dominant noise levels are expected to arise from the blade thickness and steady loading and to have azimuthal symmetry. Contour plots showing the noise radiation patterns for the four-bladed SR propeller at $\alpha = 0°$ are given in figure 8. Part (a) of the figure contains the OASPL radiation patterns measured for the two low tip speeds (runs 52 and 53). Here the individual harmonic levels are not presented because these operating conditions produced propeller noise levels about the same as the background noise level. The resultant radiation patterns are somewhat irregular. The second harmonic levels were much below those of the first harmonic (fundamental, or BPF), so that the spatial distribution and levels of the OASPL are the same as those of the first harmonic. The data indicate that the highest noise levels occur in the propeller plane and decrease upstream and downstream from that plane. Figure 8(b) shows the data for the high tip speeds (runs 54 and 55). Here the spatial distributions of the OASPL and first four harmonics of the BPF are given. In contrast to low-tip-speed operation, these levels were much above the tunnel noise and as a result are showing a more regular and symmetric pattern. Again the noise maximum occurs in the plane of the propeller and decreases upstream and downstream from this plane. This characteristic is also apparent in all the harmonics. Further, the harmonic levels decrease in level monotonically with increasing harmonic number. These characteristics of steadily loaded SR propellers are well known; they are presented here to provide a comparison for the unsteadily loaded cases to be introduced in this paper.

Pylon-mounted, four-bladed SR propeller. The noise radiation pattern for the pylon-mounted SR tractor (runs 144 and 145) are shown in figure 9. These high-tip-speed data may be compared with those of figure 8(b) to show the effect of the pylon on the noise radiation patterns. Over a large part of the measurement range, essentially no major changes are observed in the radiation pattern. The exception occurs in the upper right and lower left corners in the OASPL and first and second harmonics of run 144, where an increase in noise is apparent. This change may be indicative of a change occurring outside the measurement range or of reflections of the propeller noise from the pylon surface.

Eight-bladed SR propeller. The high-tip-speed runs that were shown in figure 9 were repeated with 8 blades (runs 141 and 142). The results are shown in figure 10. In general, the eight-bladed propeller produced in-plane values of OASPL which are about 3 dB lower than the four-bladed propeller and which decrease more rapidly upstream and downstream from that point. At first it may seem contradictory that addition of more sources (blades) decreases the noise. The explanation follows. First, it has been argued from superposition and demonstrated experimentally in reference 13 that the noise from an eight-bladed propeller can be obtained from the even harmonics of a four-bladed propeller. The first harmonic levels of the eight-bladed propeller are obtained by adding 6 dB to the pressure levels of the second harmonic of the four-bladed propeller. Similarly, the second harmonic levels of the eight-bladed propeller are obtained from the fourth harmonic of the four-bladed propeller after adding 6 dB. The data from this experiment also confirm these results if figure 9 is compared with figure 10. Second, the noise energy in the odd harmonics of the four-bladed propeller cancel because of the symmetry introduced with the addition of four more blades. Again, this property of steadily loaded propellers has been demonstrated, but these results are presented for comparison with the CR propellers, in which the total number of blades is the same.

CR propeller. The spatial distribution of the noise from the CR propeller is shown in figure 11. Part (a) presents the low-tip-speed data (runs 82 and 83) and part (b), the high-tip-speed data (runs 84 and 85). In part (a) the noise levels were recorded at two additional forward locations corresponding to 72° and 78° upstream of the propeller plane (refer to fig. 6). The spatial characteristics greatly differ from those of the SR propeller. First, for the low tip speeds, the lowest values of the OASPL appear in the plane of the propellers and then increase in both the upstream and the downstream direction. The in-plane levels (88 dB for run 82 and 98 dB for run 83), however, correspond to the in-plane levels of the four-bladed SR propeller at the low tip speeds shown in figure 8(a) (runs 52 and 53). The large increase in noise in the axial directions is attributed to the unsteady loading noise produced by the wakes of the first row of blades intersecting the

second row of blades. The harmonic decomposition of the OASPL supports this conclusion. That is, the spatial distributions of the harmonics show that the second and fourth harmonics contribute most of the axial noise to the OASPL. These even harmonics correspond to the wake-cutting frequencies of the second row of blades. The increase in the axial directions was demonstrated analytically by Runyan (ref. 6). For a steadily loaded propeller, there is theoretically no axial component.

One further observation may be made regarding the axially radiating component. The flyover angle (θ) at which these levels become a dominant noise source depends on the harmonic and on the operating conditions. For the low tip speeds the axial levels become significant in the second harmonic about 30° upstream of the propeller plane and after 30° downstream. These angles for the fourth harmonic are from 60° to 70° upstream and from 40° to 50° downstream. For the high-tip-speed data displayed in figure 11(b), these angles are larger, that is, further away from the propeller plane. Here, the axial component is not apparent in the second harmonic until about 50° in front of the disk plane and about 40° behind. The fourth harmonic axial levels are not within the measurement range.

A second contrast to the SR noise radiation patterns is the horizontal or streamwise stripes that appear in the OASPL and odd harmonics. These stripes are more apparent in the high-tip-speed data displayed in figure 11(b). Under these operating conditions, the streamwise stripes are very apparent in the OASPL patterns and indicate a change in the dominant noise mechanism. The harmonic decomposition of the noise indicates that these stripes are composed of "islands" of high noise levels. The first harmonic shows a single set and the third harmonic shows a double set that extends further upstream and downstream. A slight skew in the first harmonic islands from upper left to lower right is observed. When added together, the first and third harmonic islands form a single stripe in the OASPL pattern. These stripes occur in directions corresponding to the crossover points of the two propeller disks, although their sources may actually occur 90° to these locations. These islands are attributed to the phase addition and cancellation of the steady components of the propeller noise. This has been borne out theoretically in reference 8 for these cases (runs 84 and 85) by simply adding the predicted complex noise spectrum from these two propellers. The predictions, which require as input the location of the crossover directions, agreed very well with these data in both level and distribution of the first harmonic islands. Even the skew in the data was reproduced in the predictions.

Finally, the surprisingly high noise levels measured for this CR propeller are thought to arise from two particular aspects of the design employed. First, both disks have straight blades. With this design the relatively straight wakes produced by the first row are encountered in a short time interval by the second row of straight blades. A swept design would spread this encounter over a longer time interval. Second, both disks had the same number of blades. With this arrangement the wake encounters occur simultaneously for all four blades. Using a different number of blades for each disk would eliminate this simultaneous encounter.

Tractor Installations at Nonzero Pitch

The microphone carriage employed in this experiment allowed the noise radiation pattern to be measured to 58° on either side of the vertical ($-58° < \phi < 58°$). An extended range of measurement locations was simulated by obtaining data for $\alpha = \pm 8°$ and noting that the relative geometry of the nacelle and microphone carriage at $\alpha = -8°$ was the same as if the nacelle had been pitched at $\alpha = 8°$ and the carriage rotated 180° about the tunnel centerline. In a like manner, the geometry with the nacelle yawed was the same as if the nacelle had been pitched and the microphones rotated through an angle of 90°. This procedure produced data extending from $\phi = -58°$ to 238° as illustrated in figure 12. Here $\phi = 0°$ is the direction of a ground observer when the propeller is flying directly overhead at $\alpha = 8°$. The $\phi = 90°$ direction corresponds to a sideline, or fuselage, observer, and the data were obtained with the propeller axis yawed (see fig. 4). The $\phi = 180°$ direction corresponds to an observer directly above the aircraft, and data were obtained with the propeller axis at $\alpha = -8°$. Data were obtained at over 400 measurement positions for theory validation (ref. 9).

SR propeller. The measured results for the SR tractor installation are shown in contour format in figure 13(a) for the low tip speeds, runs 63 and 64 for $\alpha = +8°$, runs 150 and 151 for $\psi = -10°$, and runs 65 and 66 for $\alpha = -8°$. Comparing these charts with those for $\alpha = 0°$ (fig. 8(a)) shows that the noise increases under the propeller ($\phi = 0°$) and decreases above it ($\phi = 180°$). For these series, the difference in level from under to above the propeller is about 9 dB for the lower tip speed, 100 rps, and 6 dB for 120 rps. The high levels at the top of the center charts, corresponding to the yawed propeller (runs 150 and 151), are attributed

to the fact the propeller was yawed 2° more than it was pitched. This was a hardware limitation. The predicted noise radiation patterns (ref. 9) for runs 63, 150, and 65 agree well with these data and also show that the maximum noise for these operating conditions occurs under the flight path ($\phi = 0°$). Further, the predictions show that the effects of unsteady loading are least on the sideline ($\phi = \pm 90°$). These noise radiation trends were also observed for the high tip speeds (runs 67, 147, and 70 and runs 68, 148, and 69) shown in figures 13(b) and 13(c). Here the radiation patterns of the first four harmonics of the BPF are displayed. Of note in these sequences is the slight rotation of the noise for the yawed propeller (runs 147 and 148) for all the harmonics. The difference in level from under to above the propeller is about 2 dB.

CR propeller. The noise radiation patterns from the CR propeller at the high tip speeds and $\alpha = \pm 8°$ are shown in figure 14. These results were obtained at the same operating conditions as run 84 shown on the left side of figure 11(b). A simple upstream rotational shift of the noise pattern is observed for $\alpha = +8°$ (run 86), and a downstream shift for $\alpha = -8°$ (run 87). For $\alpha = -8°$ (run 87), the axially radiating component shifts into the measurement range of the microphone carriage, whereas this component is only slightly visible for $\alpha = 0°$ (run 84). There is no consistent change in level from under the propeller ($\phi = 0°$) to above it ($\phi = 180°$).

SR Pusher Installation

The effect on the noise of introducing a single wake into an operating SR propeller is shown in figure 15. Part (a) of the figure is for low-tip-speed operation, and part (b), for high-tip-speed operation. The physical location of the propeller has shifted downstream considerably in these plots because of the rotation of the nacelle about the pylon axis (see fig. 3) for the pusher operation. In figure 15(a) the OASPL data show a large upstream or axially radiating component of the noise which is not present in the tractor installation (refer to fig. 8(a)). This component adds from 5 to more than 15 dB to the SR tractor OASPL in the forward direction. In the plane of the propeller the noise increases from 2 to 5 dB with the introduction of the wake; however, most of the increase occurs in the first harmonic. The axial increase is distributed throughout the first four harmonics. For the third and fourth harmonic there is relatively no contribution to the OASPL in the plane of the propeller while significant levels of noise are measured upstream. In fact, these higher harmonics significantly contribute to the OASPL; in contrast to the contributions of the harmonics for the tractor installation. These trends are observed for the high tip speeds (runs 132 and 133) shown in figure 15(b). Here, the operating conditions correspond to those of the tractor installation shown in figure 8(b). The unsteady loads that are introduced by the wake do not appear to significantly change the in-plane levels of any of the harmonics. Their main contribution to the propeller noise over this measurement range occurs in the upstream direction. The radiation characteristics for this axially radiating sound is similar to that of the CR propeller (compare figs. 11(a) and 15(a)). Like the CR propeller, the spatial extent of the axial component varies with operating condition and harmonic number.

To further examine the noise characteristics of a propeller ingesting a wake, one can compare the averaged measured pressure time history and spectra of a microphone in the plane of the propeller with one upstream in the region of high axial noise radiation. This comparison is given in figure 16 for a high tip speed (run 132). The top trace was measured in the center of the tunnel (microphone 6, see fig. 4) slightly after the propeller plane ($\theta = -4.7°$). The waveform closely resembles a typical SR tractor waveform. The lower trace, which was measured 67.1° upstream of the propeller displays several spikes. It is conjectured that these spikes arise from the changing pressure on the propeller blades as they go through the wake. The differences in the frequency domain are shown in figure 16(c). Whereas the color contour charts show the levels of the first four harmonics of the data, here the spectral levels are shown up to the fifteenth harmonic of the BPF. The comparison shows that significant increases in the levels of high frequency noise are found in the upstream region as compared with the in-plane region, particularly in the fourth through the tenth harmonic. Thus, the axial component of the noise has higher harmonic content.

Conclusion

A movable microphone carriage permitted details of the noise radiation patterns to be measured for a representative set of propeller installations including a counter-rotation propeller.

The noise directivity characteristics for the counter-rotation (CR) propeller differed from the single-rotation (SR) propeller in two respects. First, an upstream radiating or axial component was observed for the CR propeller, the spatial extent of which varied with operating condition and frequency. Most of the axial noise energy was contained in the second and fourth harmonics of the blade passage frequency (BPF). The source of this noise is attributed

to the wakes from the first row of blades producing unsteady loads on the second row of blades. Second, in the region about the disk plane, islands of high noise radiation were observed in the odd harmonics of the BPF which contributed to streamwise stripes of high noise radiation in the overall sound pressure level (OASPL). The azimuthal location of these stripes corresponded to the crossover directions of the two sets of propeller blades. The source of these islands is attributed to the phase addition and cancellation of the steady sources of propeller noise.

For an SR propeller at nonzero pitch, the noise radiation patterns indicate that at a positive pitch angle the noise levels increase under the propeller (ground observer, $\phi = 0°$) and decrease above it ($\phi = 180°$). The difference in noise level from above to below the propeller varied from 2 to 8 dB, depending on the propeller operating conditions. For a CR propeller at nonzero pitch a difference in noise level from under to above the propeller was not as apparent as for the SR propeller. What was apparent was a simple rotational shift of the axially radiating components by an amount which corresponded to the change in pitch.

For an SR propeller in a pusher configuration, the changes in the noise characteristics from those of an SR tractor configuration are twofold. First, the noise radiation patterns show that the pusher is slightly noisier in the propeller plane (2 to 5 dB) and considerably noisier upstream (5 to more than 15 dB). The increase in noise level and the directivity of the OASPL and harmonics of the BPF depend on the propeller operating conditions and harmonic number. Second, the wake introduces spikes into the average pressure time history, which produce higher noise levels from the fourth to the tenth harmonic. These spikes become increasingly evident as the observer moves from the propeller plane toward the propeller axis.

NASA Langley Research Center
Hampton, VA 23665-5225
December 11, 1985

References

1. Mitchell, Glenn A.; and Mikkelson, Daniel C.: *Summary and Recent Results From the NASA Advanced High-Speed Propeller Research Program.* NASA TM-82891, [1982].
2. Tanna, H. K.; Burrin, R. H.; and Plumblee, H. E., Jr.: Installation Effects on Propeller Noise. *J. Aircr.*, vol. 18, no. 4, Apr. 1981, pp. 303-309.
3. Herkes, W.: *An Experimental Study of the Noise Generated by a Pusher Propeller Due to a Wake Entering the Propeller Disc.* EOARD-TR-80-5 (Contract AFOSR 79-0033), Nov. 5, 1979. (Available from DTIC as AD A078 437.)
4. Block, P. J. W.: *Analysis of Noise Measured From a Propeller in a Wake.* NASA TP-2358, 1984.
5. Hubbard, Harvey H.: *Sound From Dual-Rotating and Multiple Single-Rotating Propellers.* NACA TN 1654, 1948.
6. Runyan, H. L.: Noise From a Vibrating Propeller. *J. Aircr.*, vol. 19, no. 6, June 1982, pp. 419-424. (Available as AIAA-80-1011.)
7. Block, P. J. W.: Noise Radiation Patterns of Counter-Rotation and Unsteadily Loaded Single-Rotation Propellers. *J. Aircr.*, vol. 22, no. 9, Sept. 1985, pp. 776-783.
8. Block, Patricia J. W.: Acoustics for Advanced Turboprop Aircraft. *Langley Symposium on Aerodynamics Volume II*, Sharon H. Stack, compiler, NASA CP-2398, 1986, pp. 59-72.
9. Padula, S. L.; and Block, P. J. W.: Predicted Changes in Advanced Turboprop Noise With Shaft Angle of Attack. *J. Propuls. & Power*, vol. 1, no. 5, Sept. Oct. 1985, pp. 381 387. (Available as AIAA-84-2347.)
10. Block, P. J. W.: *Installation Noise Measurements of Model SR and CR Propellers.* NASA TM-85790, 1984.
11. Block, P. J. W.; and Gentry, Garl L., Jr.: *Evaluation of the Langley 4- by 7-Meter Tunnel for Propeller Noise Measurements.* NASA TM-85721, 1984.
12. Cline, A. K.: Scalar- and Planar-Valued Curve Fitting Using Splines Under Tension. *Commun. ACM*, vol. 17, no. 4, Apr. 1974, pp. 218-220.
13. Brooks, Bennett M.; and Metzger, F. B.: *Acoustic Test and Analysis of Three Advanced Turboprop Models.* NASA CR-159667, 1980.

TABLE 1. SPINNER AND NACELLE COORDINATES
FOR SINGLE-ROTATION PROPELLER

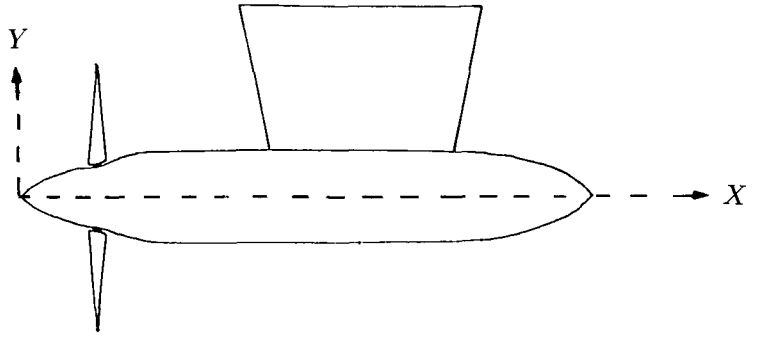

X		Y	
inches	meters	inches	meters
0	0	0	0
.25	.006	.375	.010
.50	.013	.563	.014
.75	.019	.750	.019
1.00	.025	.875	.022
1.50	.038	1.125	.029
2.00	.051	1.344	.034
2.50	.064	1.500	.038
3.00	.076	1.656	.042
3.50	.089	1.781	.045
4.00	.102	1.875	.048
4.50	.114	1.906	.048
5.00	.127	2.000	.051
5.50	.140	2.200	.056
6.00	.152	2.380	.060
6.50	.165	2.563	.065
7.00	.178	2.719	.069
8.00	.203	2.925	.074
9.00	.229	3.000	.076
28.70	.729	3.000	.076
29.00	.737	2.981	.076
30.00	.762	2.937	.075
31.00	.789	2.825	.072
32.00	.813	2.669	.068
33.00	.838	2.489	.063
34.00	.864	2.213	.056
35.00	.889	1.906	.048
36.00	.914	1.456	.037
37.00	.940	.844	.021
37.72	.958	0	0

TABLE 2. CONFIGURATION DESCRIPTION AND TEST CONDITIONS

Run	Mount	Installation	Propeller type	No. of blades	$\beta_{.75}$, deg	Speed, rps	Nacelle attitude, deg		Maximum color scale level, dB
							Pitch, α	Yaw, ψ	
52, 53	Sting	Tractor	SR	4	20.6	100, 120	0	0	100, 105
54, 55					12.7	168, 190	0	0	110, 120
63, 64					20.6	100, 120	8	0	100, 105
65, 66						100, 120	−8	0	100, 105
67, 68					12.7	168, 190	8	0	110, 120
69, 70						190, 168	−8	0	120, 110
82, 83			CR	4 + 4	21.3	100, 120	0	0	110, 115
84, 85					13.3	168, 190	0	0	120, 120
86						168	+8	0	120
87						168	−8	0	120
132, 133	Pylon	Pusher	SR	4	12.7	168, 190	0	0	110, 120
134, 135					20.6	100, 120	0	0	100, 105
141, 142		Tractor	SR	8	12.7	168, 190	0	0	110, 120
144, 145				4	12.7	168, 190	0	0	
147, 148						168, 190	0	−10	110, 120
150, 151					20.6	100, 120	0	−10	100, 105

TABLE 3. PROPELLER OPERATING CONDITIONS

Rotational speed, rps	Advance ratio		Helical tip Mach no.		Thrust,[b] lbf (N)	C_T
	SR	CR[a]	SR	CR[a]		
100	0.710	0.745	0.408	0.389	15.9 (70.7)	0.168
120	.592	.621	.486	.463	26.1 (116.1)	.192
168	.423	.444	.674	.643	15.2 (67.6)	.057
190	.374	.392	.761	.725	26.2 (116.5)	.077

[a]The smaller propeller diameter for the CR propeller results in higher advance ratios and smaller helical tip Mach numbers.

[b]Averaged measured values for the four-bladed SR propeller at $\alpha = 0°$.

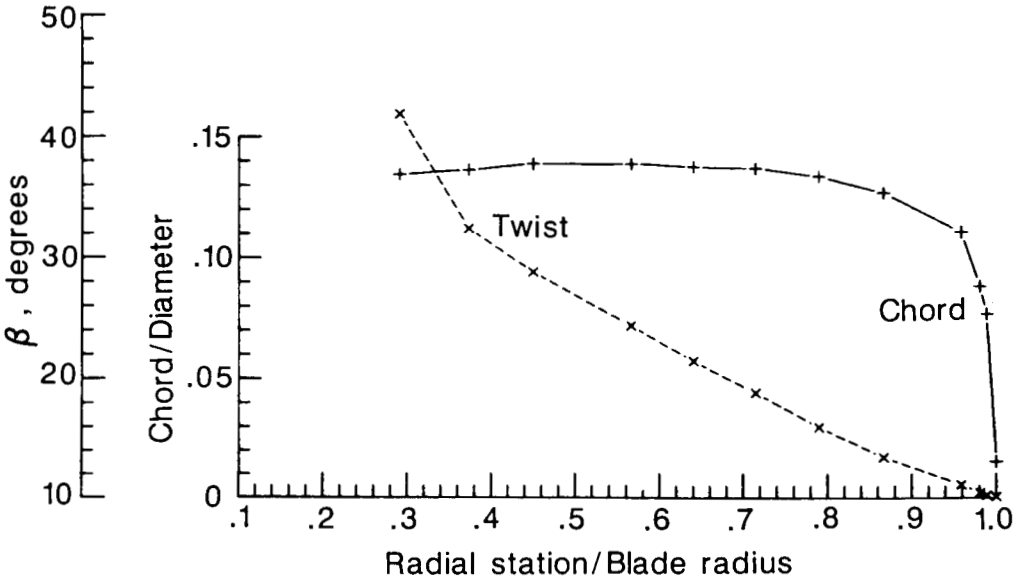

Figure 1. Chord and twist distribution for the SR-2 propeller.

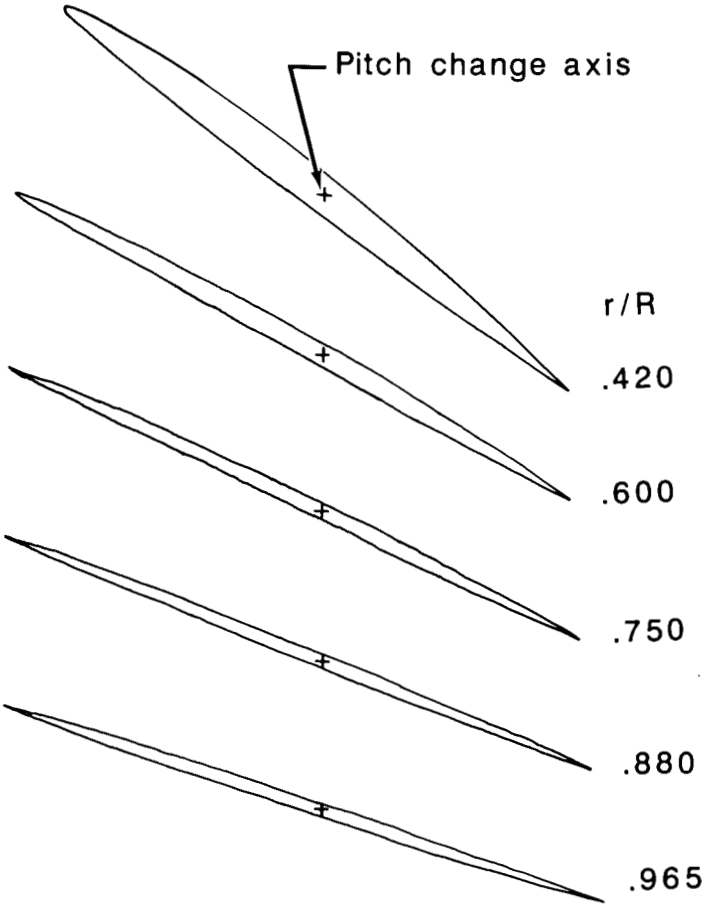

Figure 2. Representative set of normalized SR-2 propeller airfoil sections.

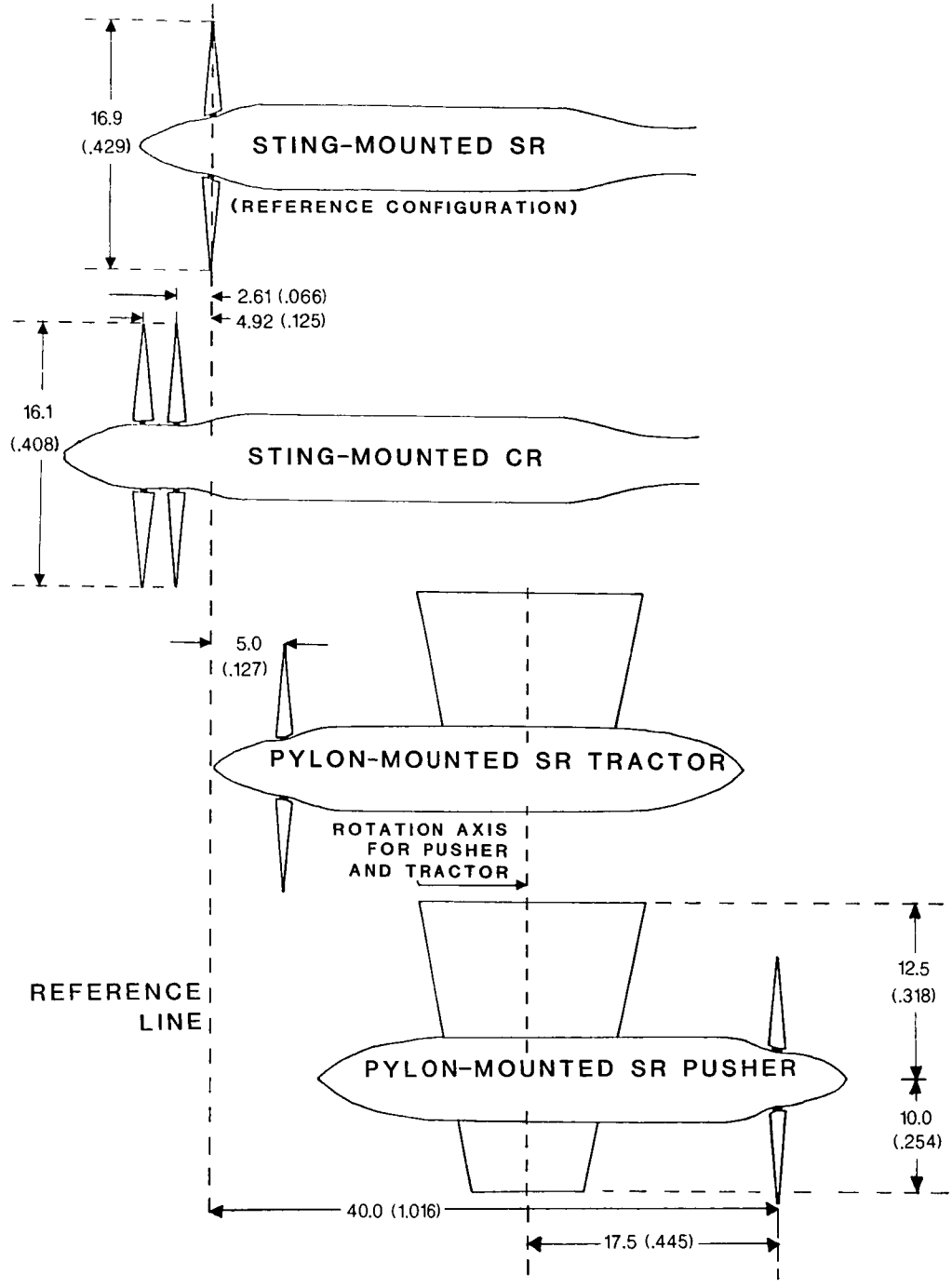

Figure 3. Propeller installations.

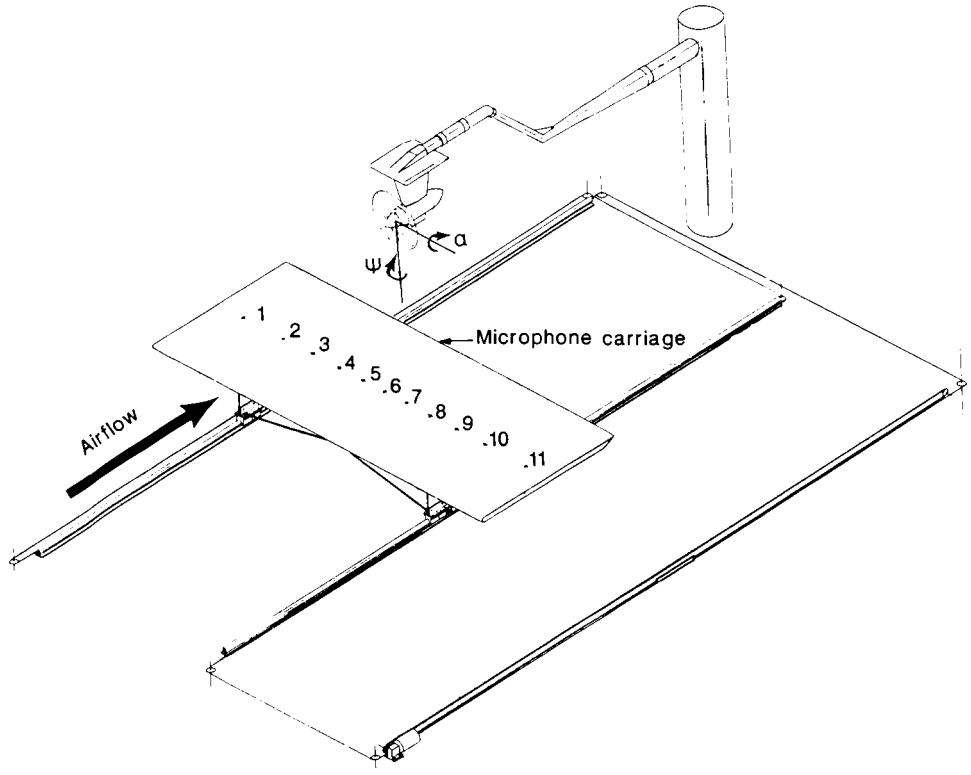

Figure 4. Isometric sketch of microphone carriage as operated for noise measurements.

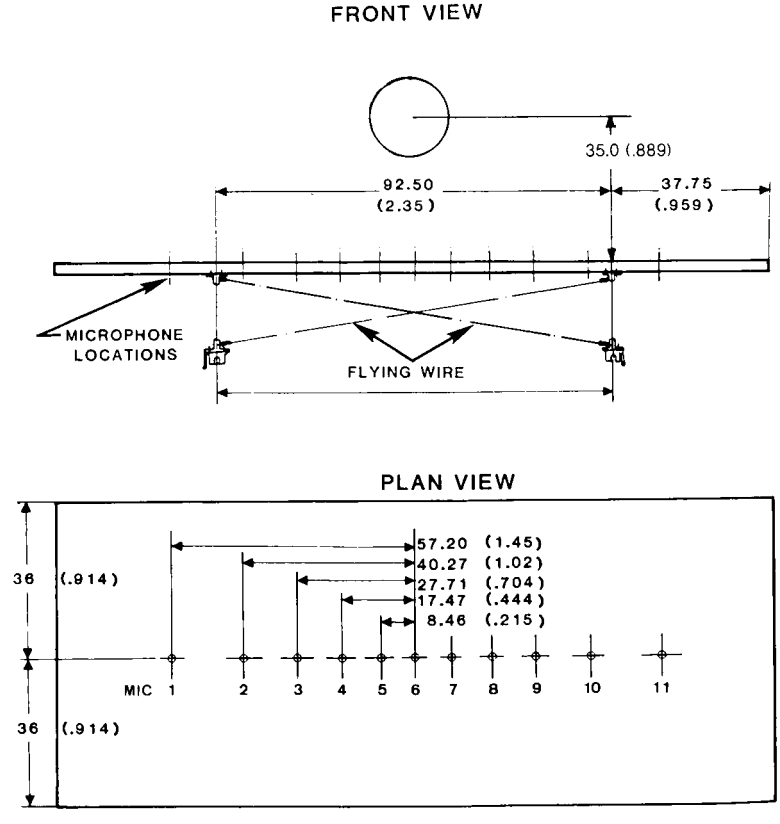

Figure 5. Plan view and front view of the microphone carriage showing propeller size and location.

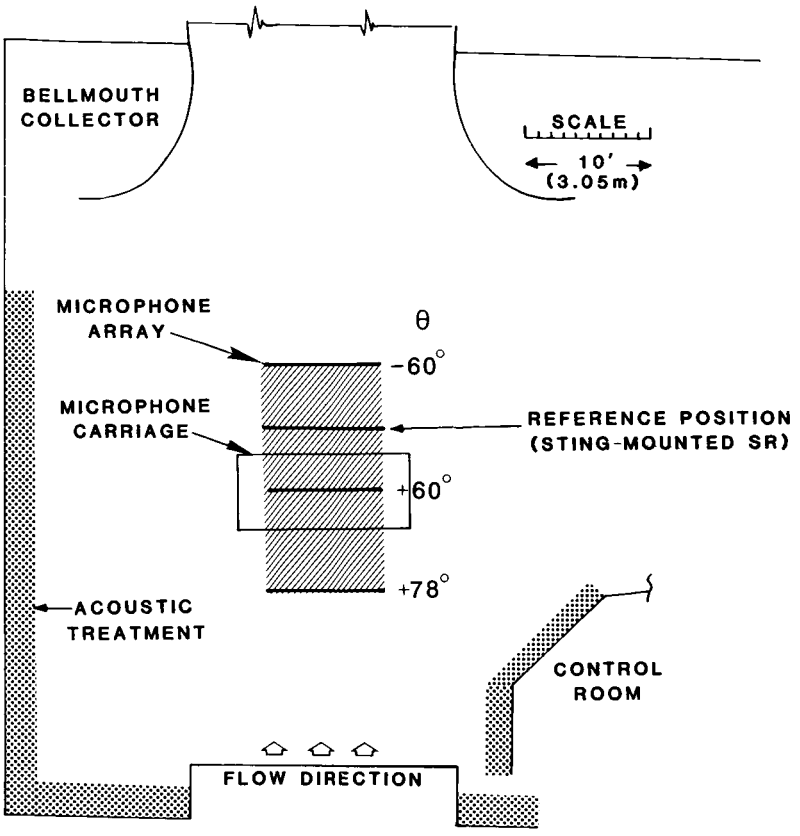

Figure 6. Plan view of the open test section of the Langley 4- by 7-Meter Tunnel showing relative size of the microphone carriage and locations of the microphone measurements.

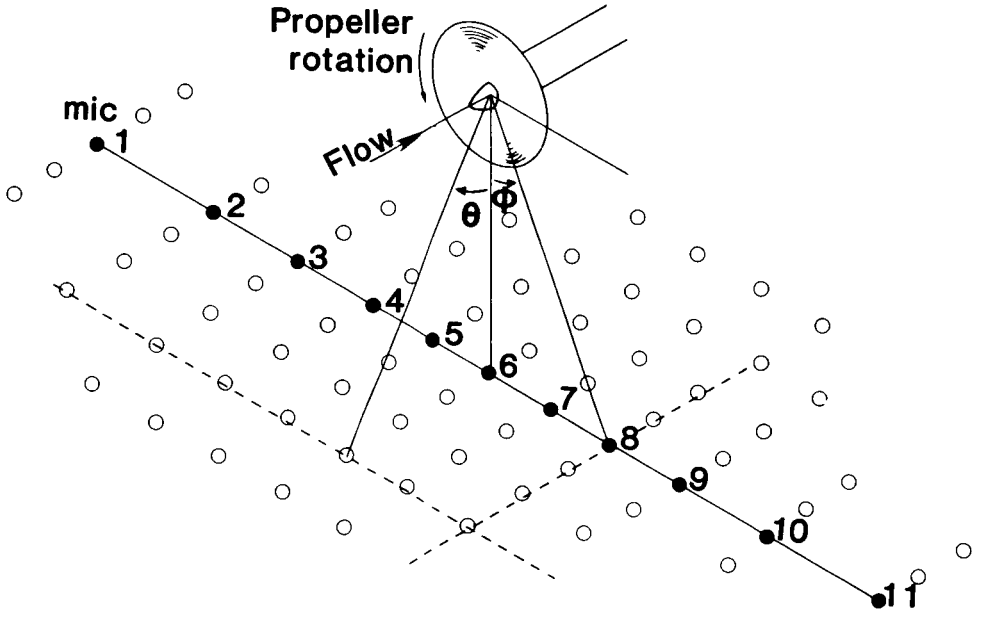

Figure 7. Sketch indicating grid of microphone locations generated by the microphone carriage and the angles of the microphone measurements, θ and ϕ.

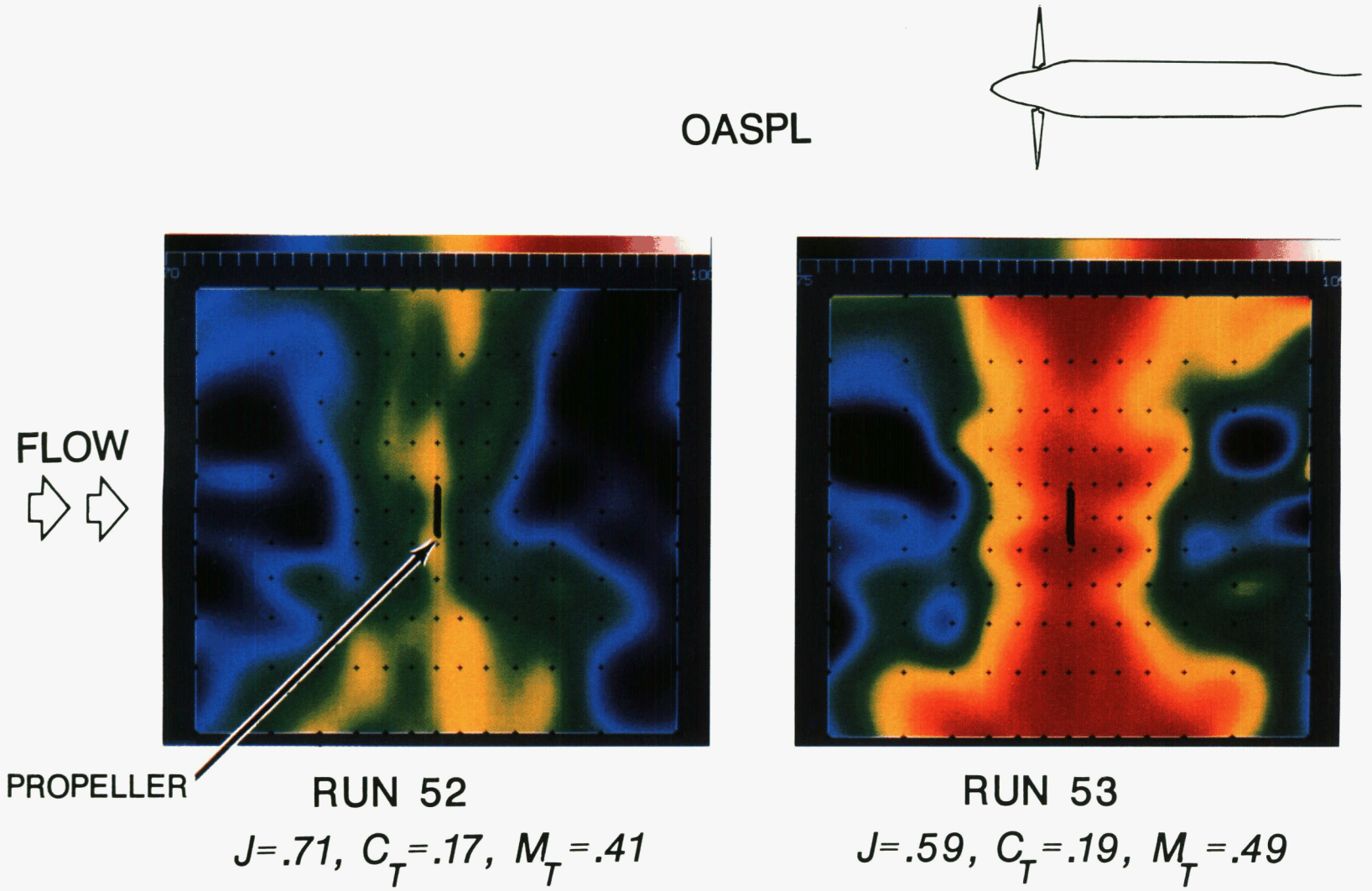

(a) Low tip speeds.

Figure 8. Noise radiation patterns for the sting-mounted four-bladed SR tractor at $\alpha = 0°$.

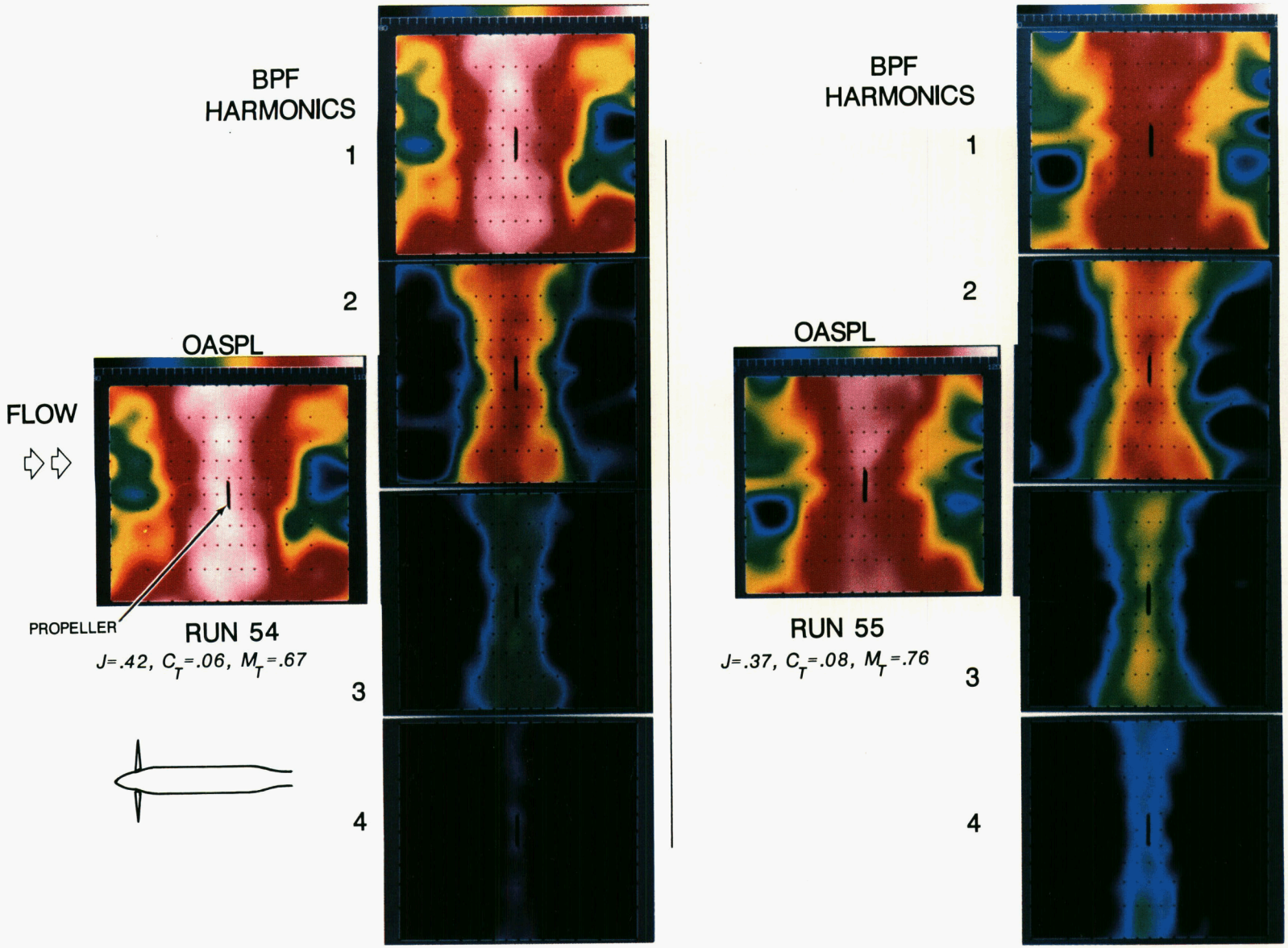

(b) High tip speeds.

Figure 8. Concluded.

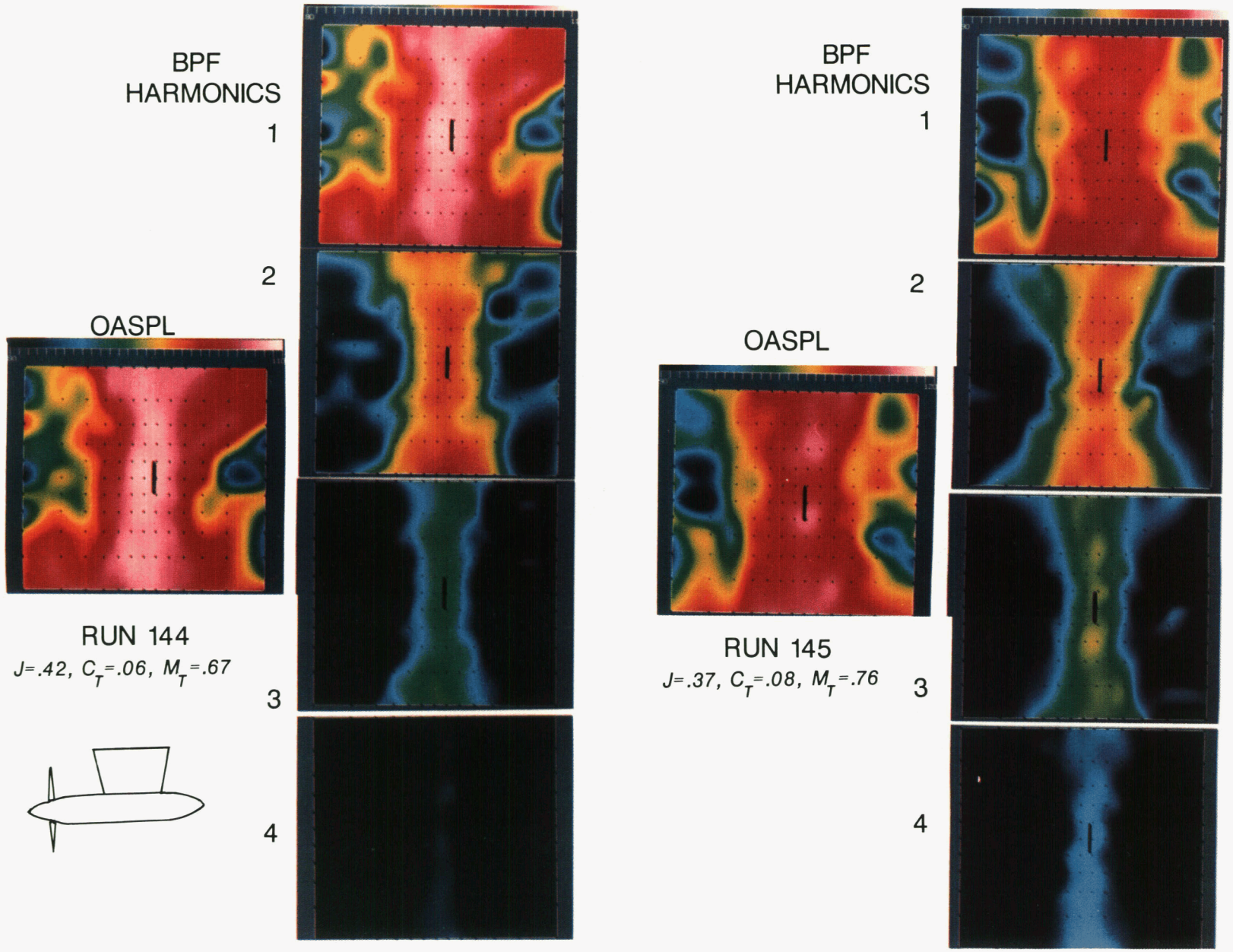

Figure 9. Noise radiation patterns for the pylon-mounted four-bladed SR tractor at $\alpha = 0°$ and high tip speeds.

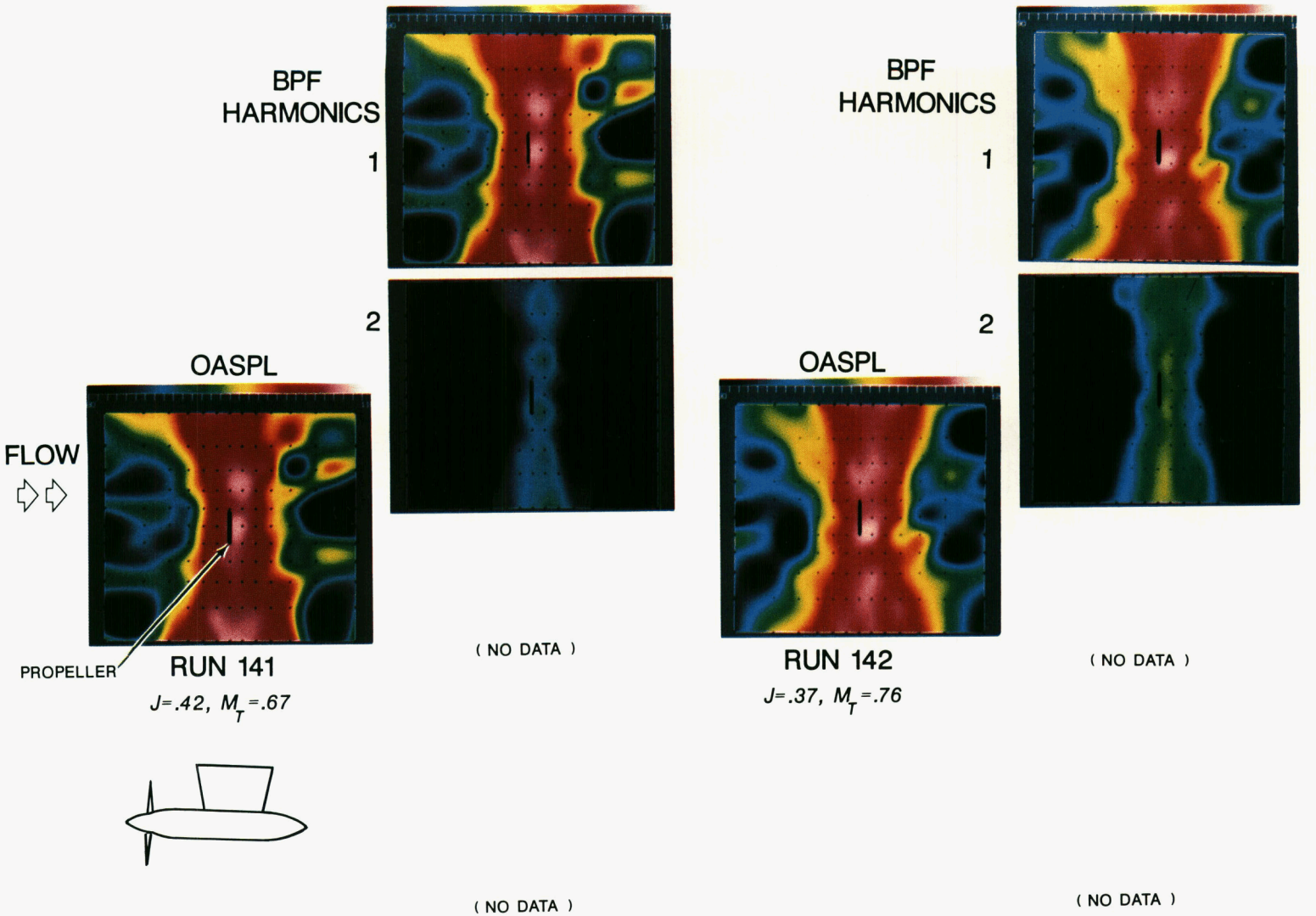

Figure 10. Noise radiation patterns for the eight-bladed SR tractor at $\alpha = 0°$ and high tip speeds.

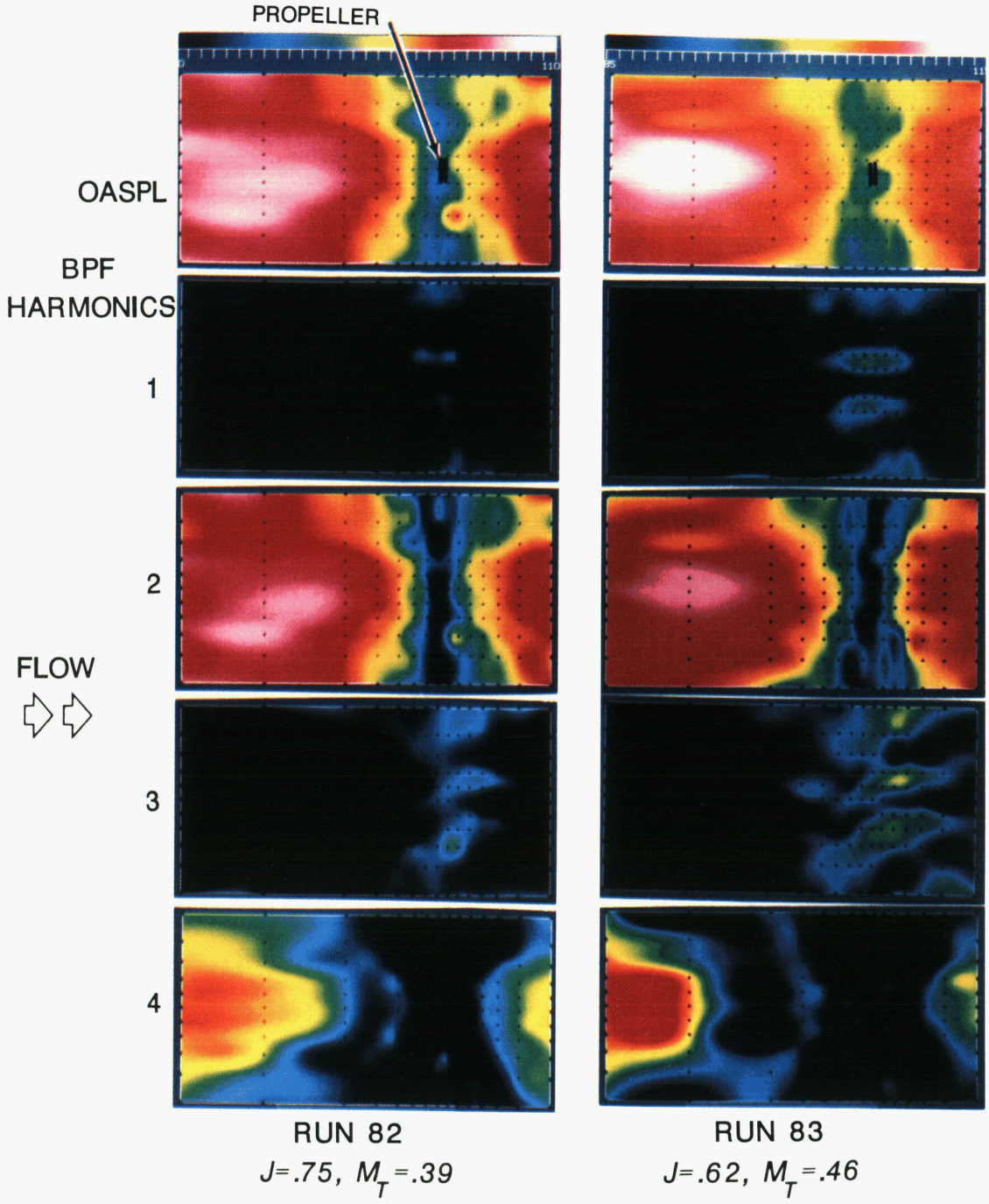

(a) Low tip speeds.

Figure 11. Noise radiation patterns for the CR tractor at $\alpha = 0°$.

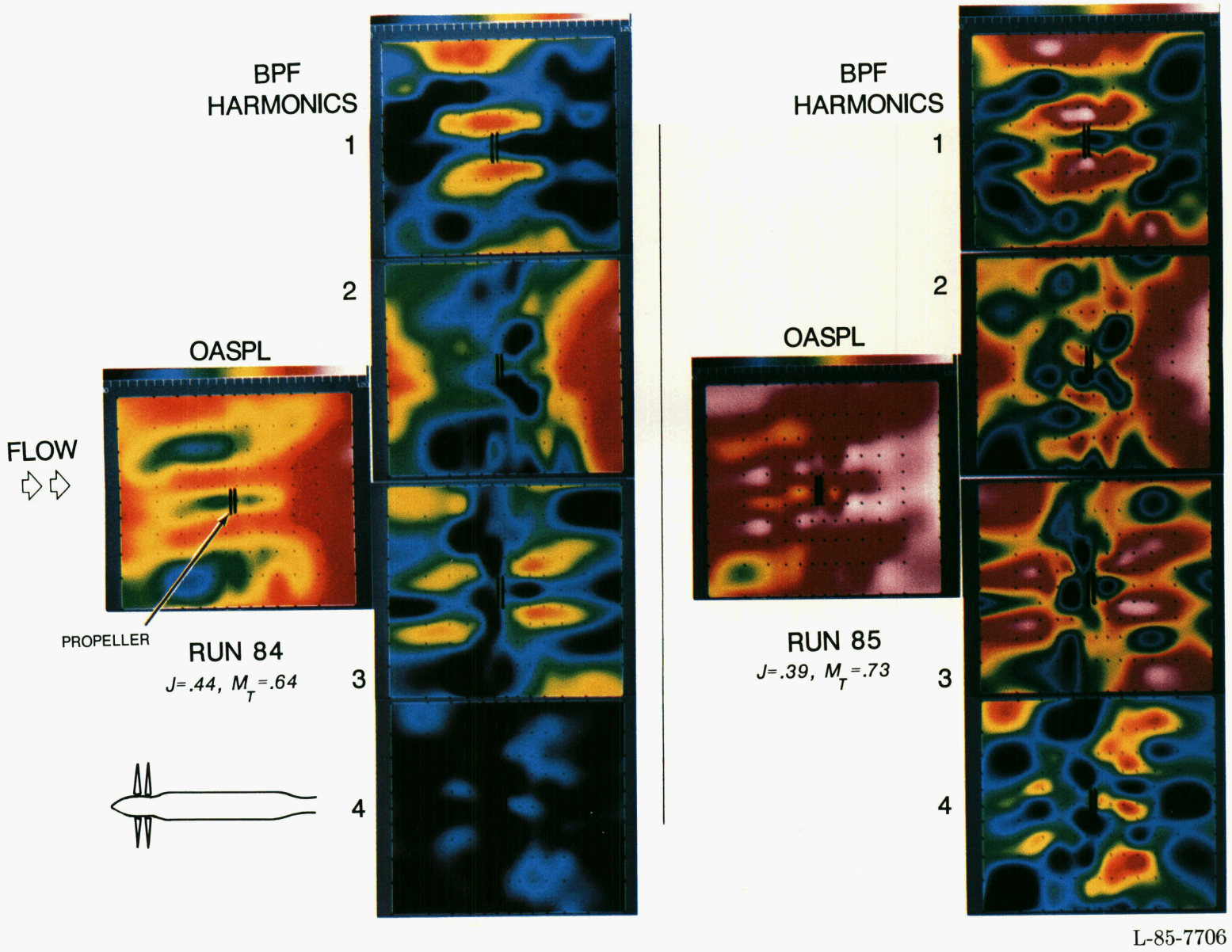

(b) High tip speeds.

Figure 11. Concluded.

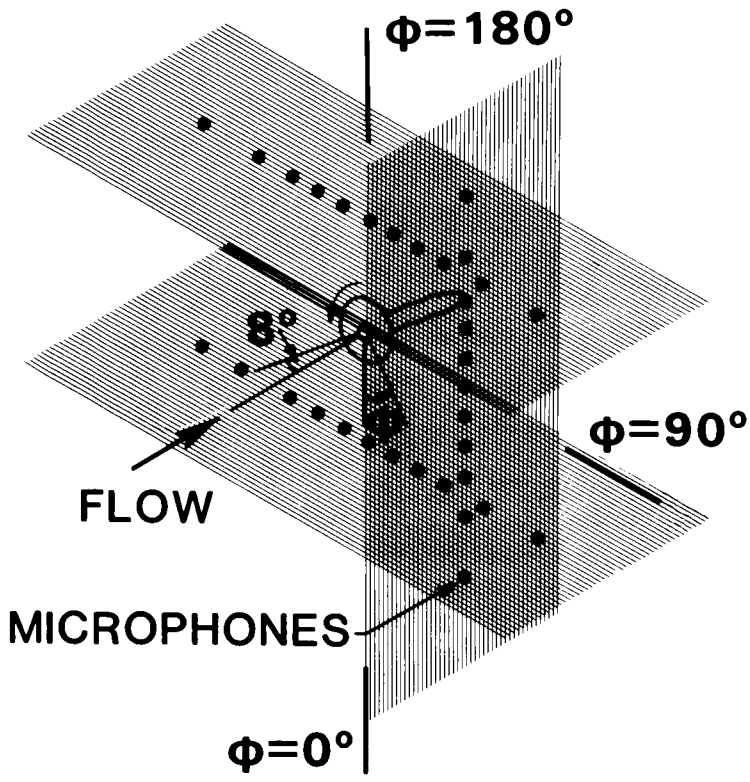

Figure 12. Sketch indicating range over which noise data were obtained for a propeller at nonzero pitch.

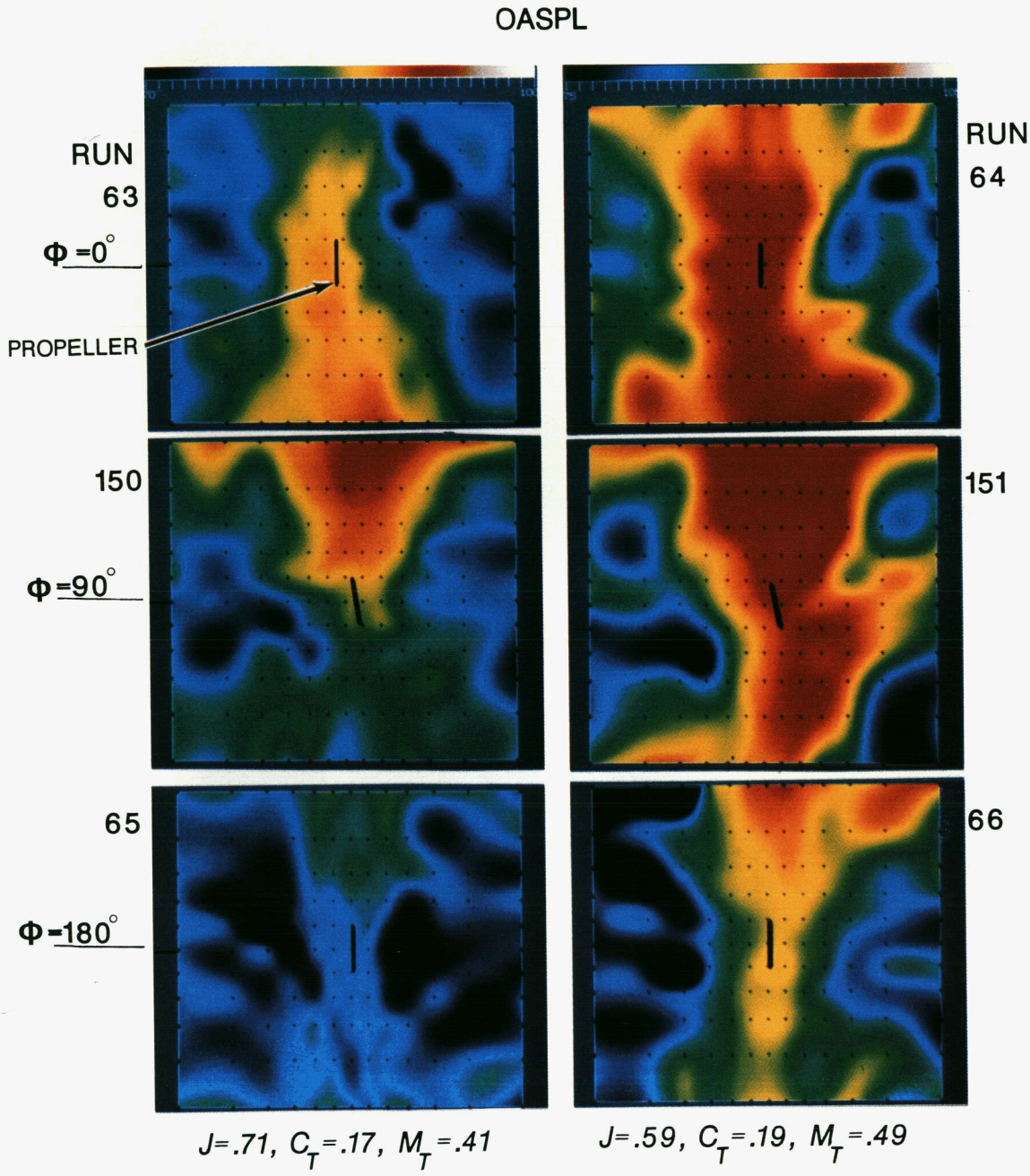

(a) Low tip speeds.

Figure 13. Noise radiation patterns for the four-bladed SR tractor at nonzero pitch.

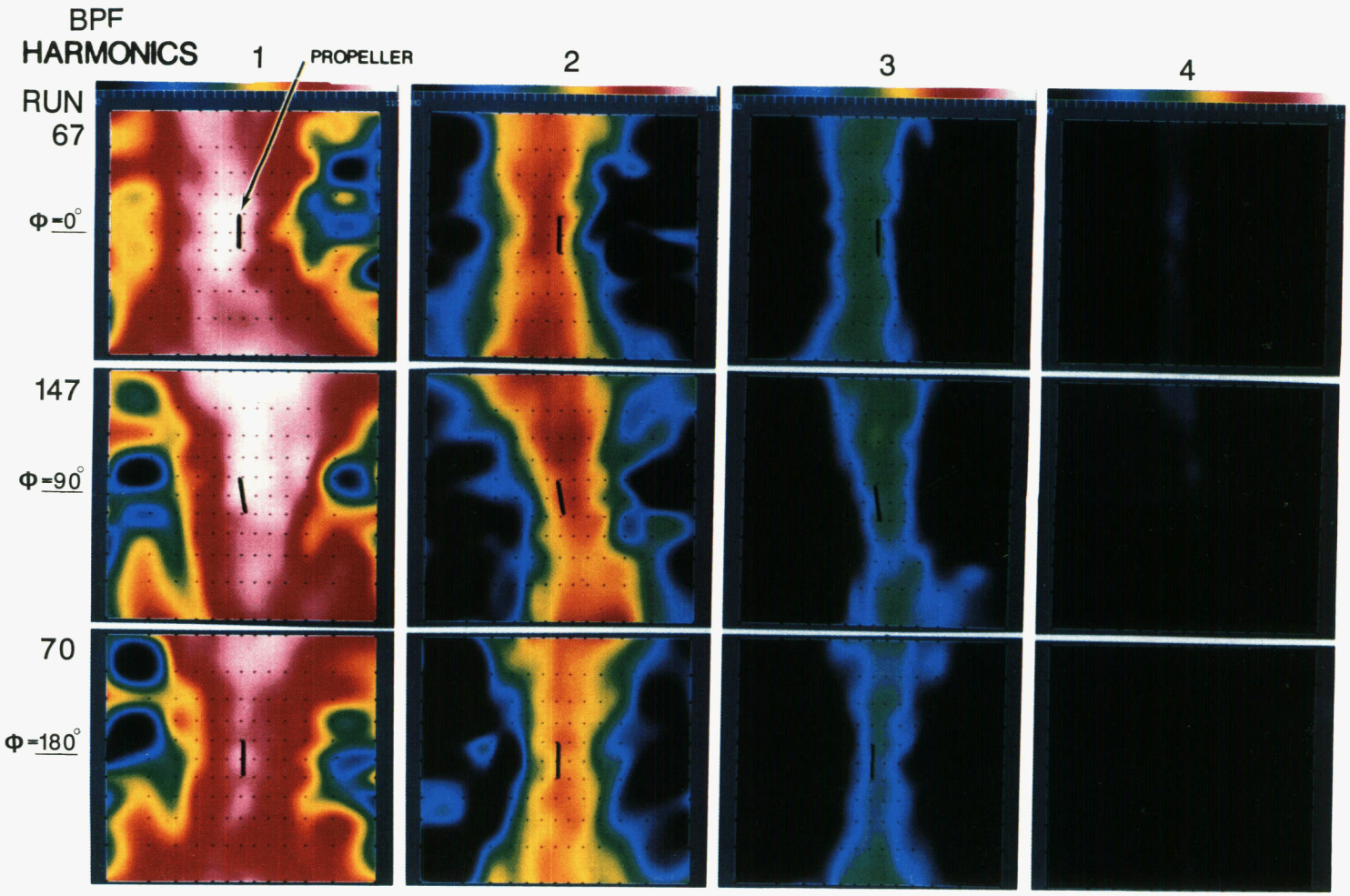

$J=.42$, $C_T=.06$, $M_T=.67$

L-85-7700

(b) High tip speed, 168 rps.

Figure 13. Continued.

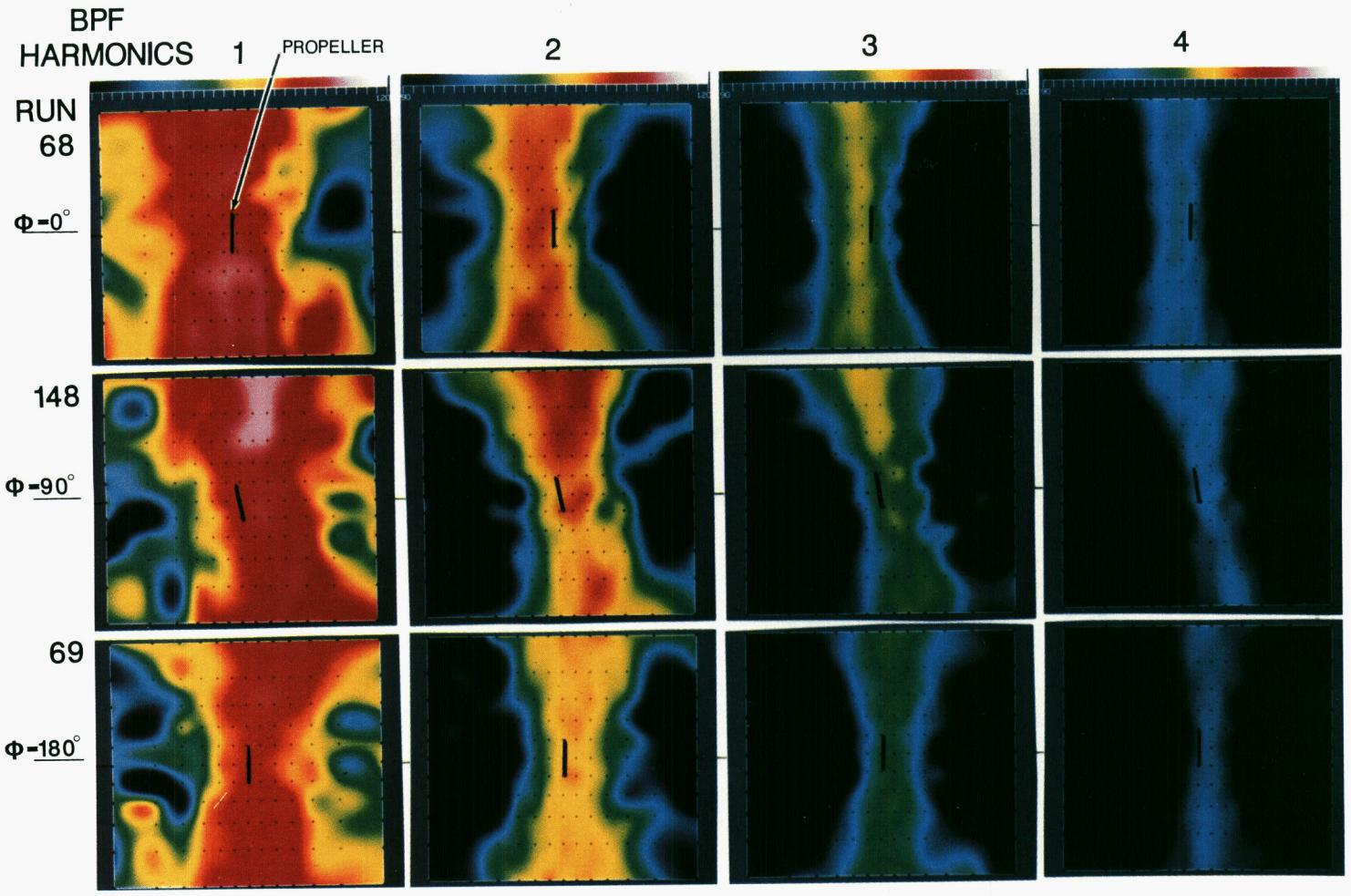

$J=.37$, $C_T=.08$, $M_T=.76$

L-85-7697

(c) High tip speed, 190 rps.

Figure 13. Concluded.

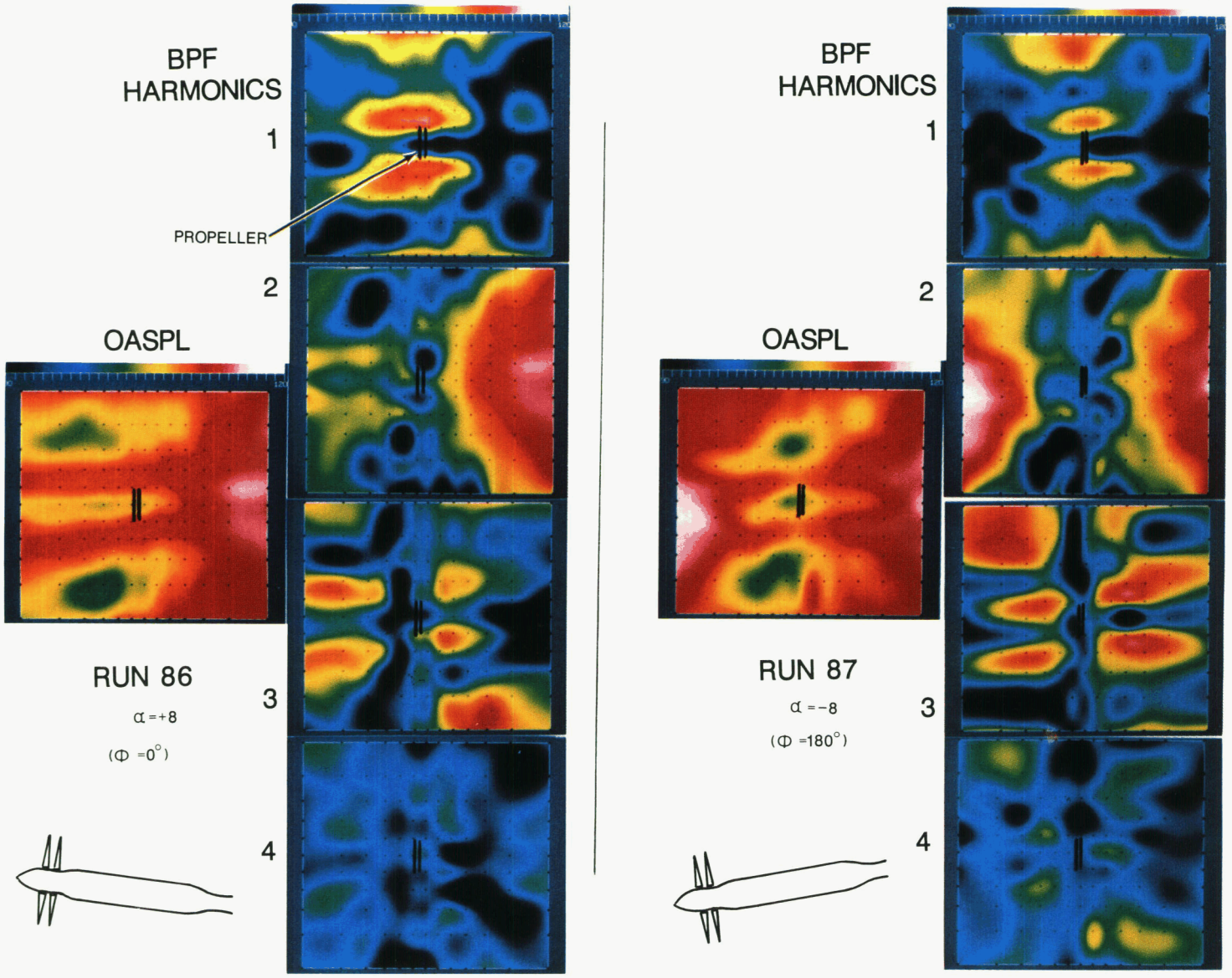

Figure 14. Noise radiation patterns for the CR tractor at nonzero pitch and high tip speeds.

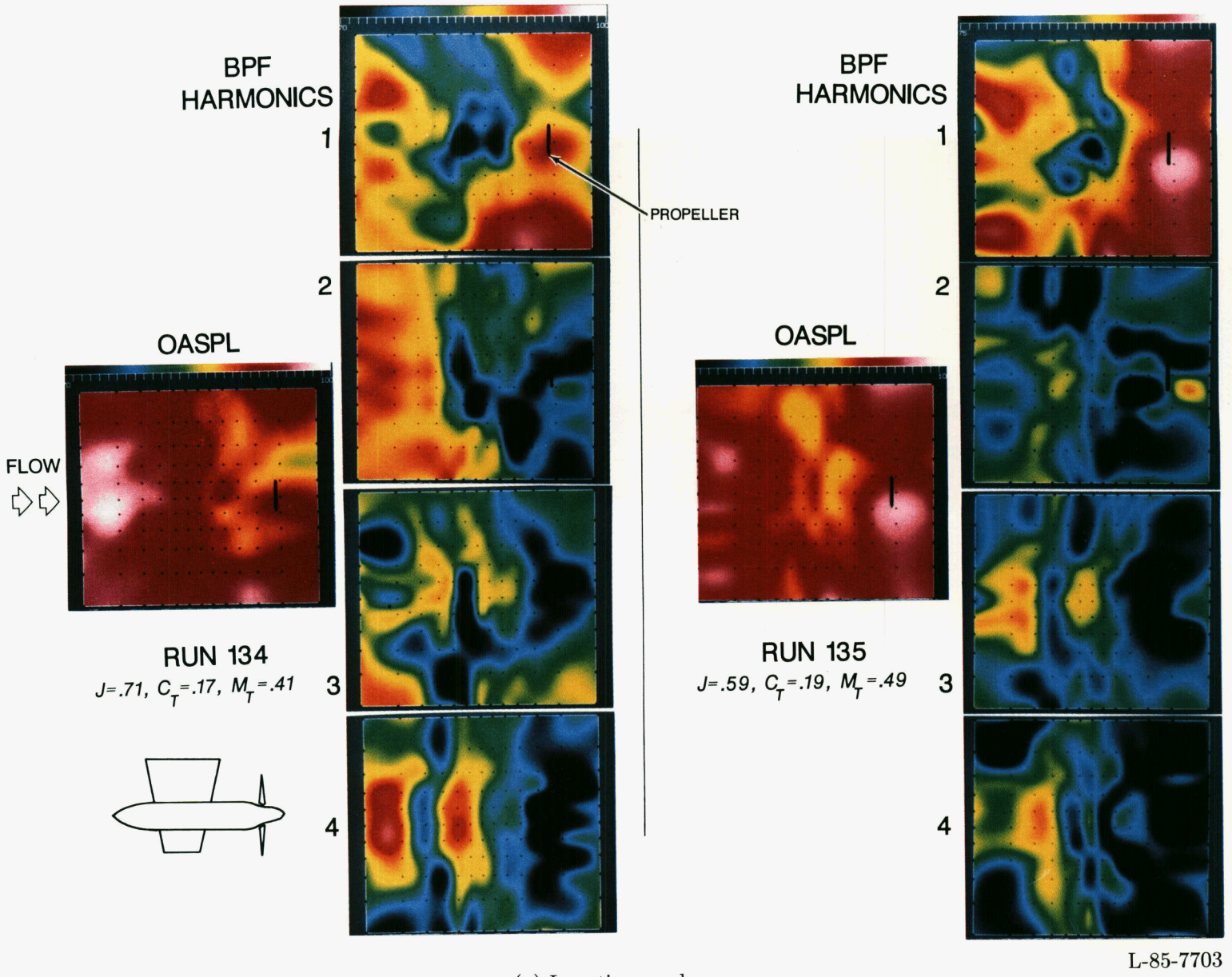

(a) Low tip speeds.

Figure 15. Noise radiation pattern for a four-bladed SR in a pusher installation.

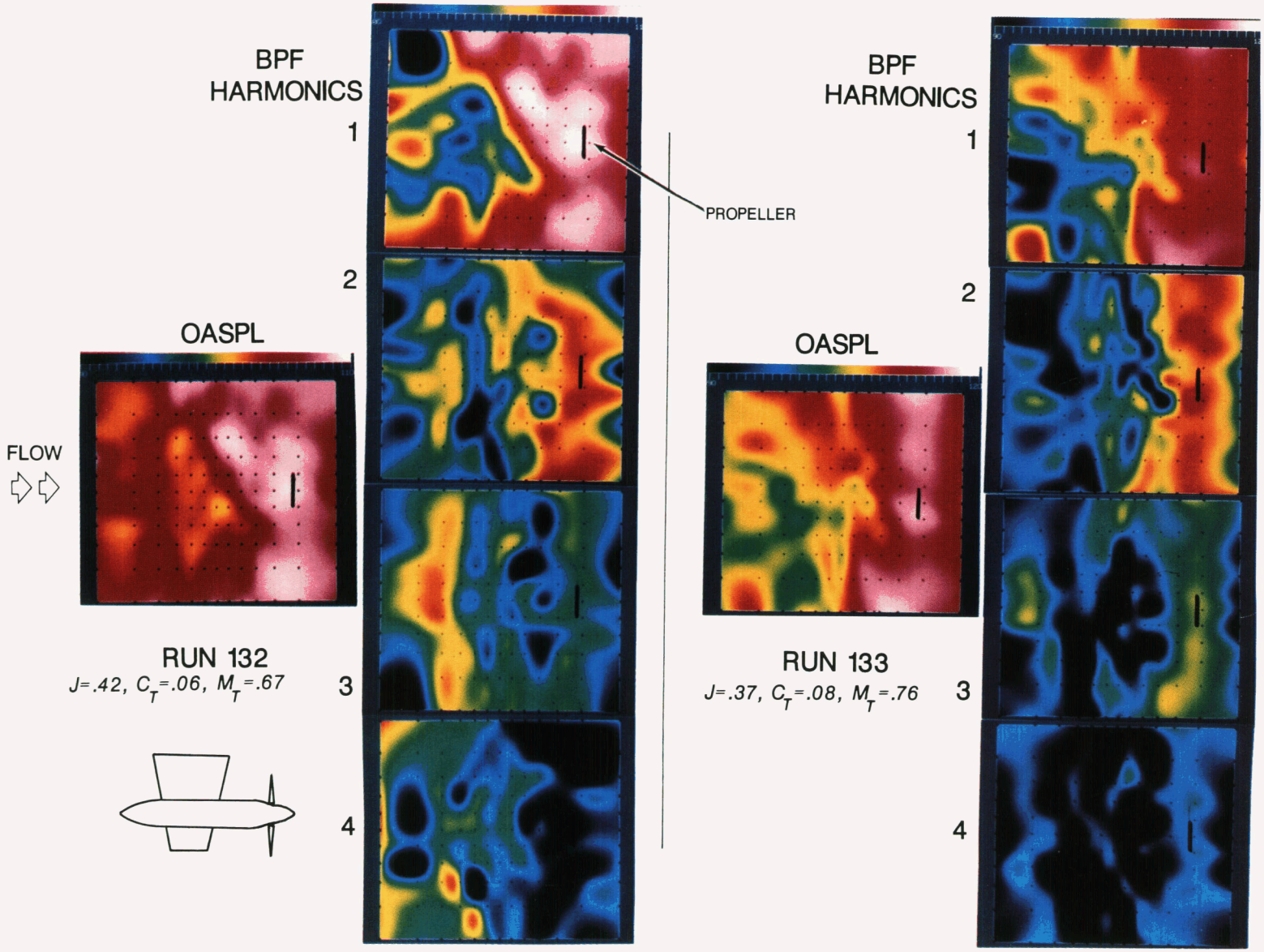

(b) High tip speeds.

Figure 15. Concluded.

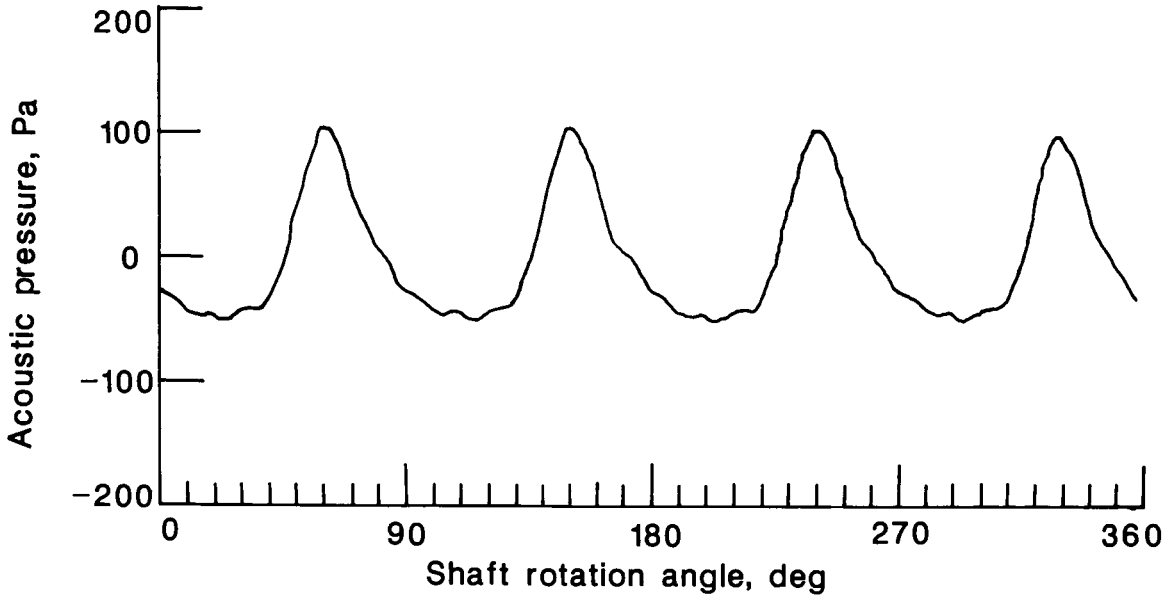

(a) Average time history in the plane of rotation ($\theta \approx 0°$).

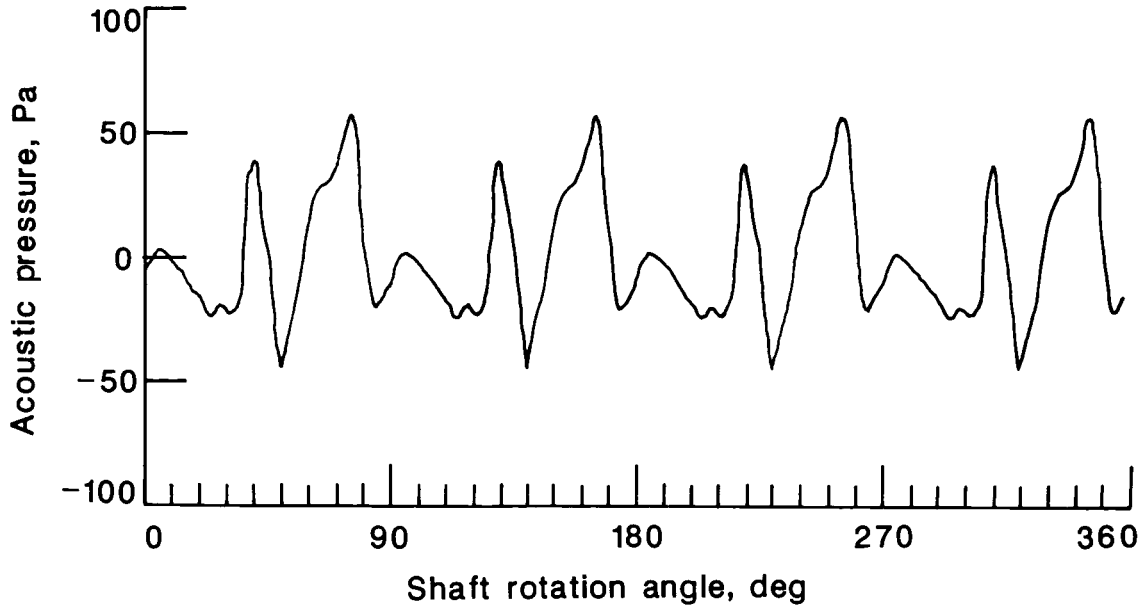

(b) Average time history upstream of propeller ($\theta \approx 67°$).

Figure 16. Comparison between the pressure time history and spectra of the tunnel centerline microphone (mic 6) close to the plane of rotation ($\theta \approx 0°$) and upstream ($\theta \approx 67°$). Run 132.

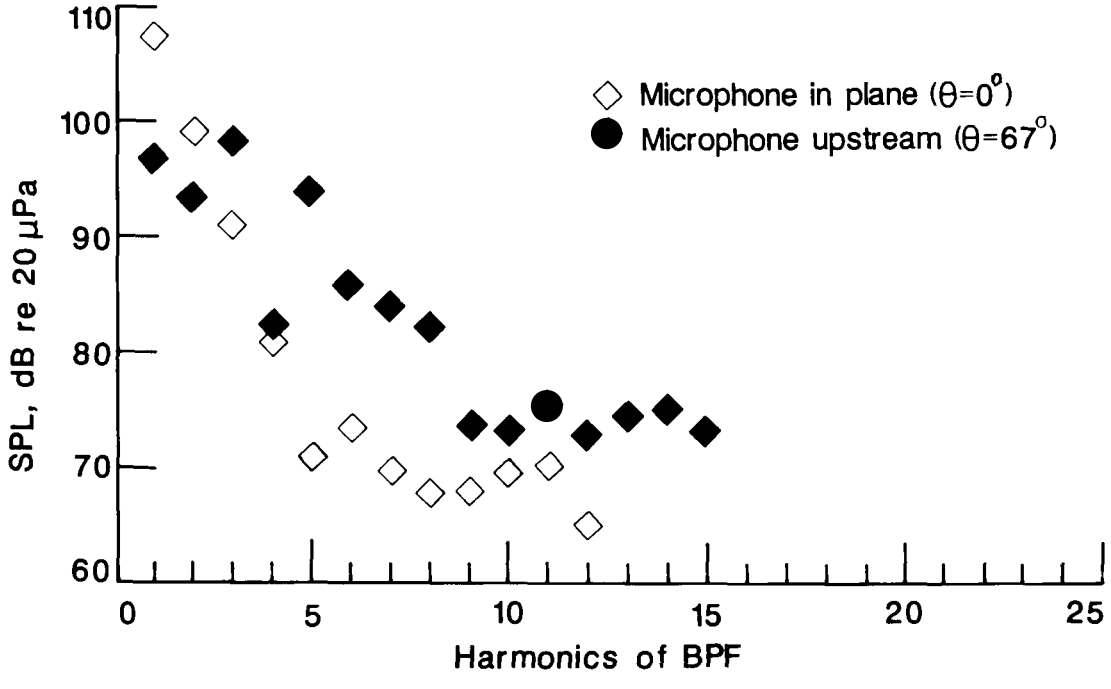

(c) Pressure spectra.

Figure 16. Concluded.

Standard Bibliographic Page

1. Report No.	2. Government Accession No.	3. Recipient's Catalog No.
NASA TP-2541		

4. Title and Subtitle	5. Report Date
Experimental Study of the Effects of Installation on Single- and Counter-Rotation Propeller Noise	April 1986
	6. Performing Organization Code: 535-03-12-11
7. Author(s): P. J. W. Block	8. Performing Organization Report No.: L-16046
9. Performing Organization Name and Address: NASA Langley Research Center, Hampton, VA 23665-5225	10. Work Unit No.
	11. Contract or Grant No.
12. Sponsoring Agency Name and Address: National Aeronautics and Space Administration, Washington, DC 20546-0001	13. Type of Report and Period Covered: Technical Paper
	14. Sponsoring Agency Code

15. Supplementary Notes

16. Abstract

To understand the effects of installation on propeller noise, numerous measurements are required to define the directivity as well as the level of the noise. An experimental study was conducted in a wind tunnel to map the noise radiation pattern for various single-rotation (SR) propeller and counter-rotation (CR) propeller installations. The measurements covered ±60° from the propeller disk plane and ±60° in the cross-stream direction. Configurations examined included SR and CR propellers at angle of attack and an SR pusher installation. The increases in noise that arise from an unsteady loading operation such as an SR pusher or a CR exceeded 15 dB in the forward axial direction and in addition strongly depended on the observer location. Most of the additional noise appears to radiate in the axial directions for unsteady loading operations of both the SR pusher and the CR tractor.

17. Key Words (Suggested by Authors(s))	18. Distribution Statement
Propellers Noise measurement Acoustic measurement Unsteady flow Wakes Pylons	Unclassified—Unlimited Subject Category 71

19. Security Classif.(of this report)	20. Security Classif.(of this page)	21. No. of Pages	22. Price
Unclassified	Unclassified	33	A03

For sale by the National Technical Information Service, Springfield, Virginia 22161

NASA-Langley, 1986